The Astrophysical Journal, 898:11 (17pp), 2020 July 20 https://doi.org/10.3847/1538-4357/ab9a51

Impact of Ordered and Disordered Magnetic Fields on Multiwavelength Emission of Blazars

Manasvita Joshi[1,2], Alan P. Marscher[1], and Markus Böttcher[3]
[1] Institute for Astrophysical Research, Boston University, 725 Commonwealth Ave., Boston, MA 02215, USA; m.joshi@northeastern.edu
[2] Research Computing, Northeastern University, 360 Huntington Ave., Boston, MA 02215, USA
[3] Centre for Space Research, North-West University, Potchefstroom Campus, Potchefstroom 2520, South Africa
Received 2018 September 10; revised 2020 May 24; accepted 2020 June 5; published 2020 July 17

Abstract

We present a detailed analysis of the effects of magnetic field topology on the spectral energy distribution (SED) and spectral variability patterns (SVPs) of blazars. In order to study these effects, we have extended our time-dependent leptonic jet model (in the internal shock scenario) to include the dependence of the synchrotron emissivity on the angle between the photon direction and the magnetic field in the plasma frame. We have explored the effects of different magnetic field geometries, such as parallel, perpendicular, oblique, toroidal, and helical, on the simulated SEDs and SVPs of a generic blazar for both purely ordered and disordered components of fields. These considerations provide either upper or lower limits to the impact on blazar emission, depending on the fraction of a disordered component present and the viewing angle. The results of our work point out some of the signatures that the orientations can leave on the SEDs and SVPs of a blazar. For example, in the case of a purely oblique field, if the magnetic field is aligned along the line of sight (in the plasma frame), it results in an annulment of the synchrotron component while keeping the flux level of the high-energy component intact. On the other hand, in the presence of a disordered component, the impact of an oblique field is reduced, and the same effect is not observed.

Unified Astronomy Thesaurus concepts: Blazars (164); Radiative processes (2055); Radiative transfer (1335); Hydrodynamical simulations (767); Relativistic jets (1390); Shocks (2086); Plasma astrophysics (1261); Active galactic nuclei (16); Radiative transfer equation (1336); High energy astrophysics (739); Radiative transfer simulations (1967); Magnetic fields (994)

1. Introduction

Blazars are well known for their photopolarimetric variability across a wide range of the electromagnetic spectrum. Many bright γ-ray blazars that are in the third Fermi-LAT source catalog (Ackermann et al. 2015) have exhibited variations in both their flux and linear polarization (e.g., Gabuzda et al. 2006; D'Arcangelo et al. 2009; Marscher et al. 2010a). Linear polarization at millimeter, infrared (IR), and optical wavelengths tends to exhibit similar position angles and sometimes cross-frequency correlation across these wave bands, often with some time delay (e.g., Gabuzda et al. 1996; Lister & Smith 2000; Jorstad et al. 2007). The degree of polarization, $P(\%)$, is generally higher at optical than at radio frequencies, implying that the optical emission originates in smaller volumes (e.g., Jorstad et al. 2013; Aleksić et al. 2014; Fraija et al. 2019). The higher polarization requires that such regions have more ordered magnetic fields than the ones responsible for radio emission. However, the impact of the magnetic ($\boldsymbol{B}$)-field geometry, as revealed by polarization measurements, on blazar jet emission has not been well studied.

Considerable effort has been put into revealing the jet's magnetic field structure and investigating the high-energy (HE) emission mechanism using multi-wave-band flux observations and optical-radio polarimetry as diagnostic tools (e.g., Aller et al. 1985; Marscher et al. 2008; D'Arcangelo et al. 2009; Homan et al. 2009). Simultaneous optical and millimeter-wave very long baseline array observations have provided evidence for partial cospatiality of optical and radio polarized emission in blazar jets, as well as intrinsic differences in these emissions (Lister & Smith 2000; Gabuzda et al. 2006; Jorstad et al. 2007). Recent multi-wave-band polarization observations of blazars reveal a preferred direction for the orientation of the $\boldsymbol{B}$-field. It maintains a toroidal pattern upstream of the core in BL Lac and the quasar PKS 1510–089 (Marscher et al. 2008, 2010a). On the other hand, polarization studies of OJ 287 indicate the presence of both a turbulent and a longitudinal $\boldsymbol{B}$-field in concentric cylindrical layers in the inner jet of the blazar (D'Arcangelo et al. 2009). Helical geometry of the $\boldsymbol{B}$-field has been inferred in many other BL Lac–type objects (Mahmud & Gabuzda 2007). Lister & Smith (2000) found that the emission regions in low optical polarization quasars tend to have a $\boldsymbol{B}$-field aligned with the axis of the jet, whereas high-polarization quasars usually have fields oriented perpendicular to the jet axis. In addition, the optical polarization of blazars can reach as high as 46% in some cases (Lister & Smith 2000). Hence, the structure and degree of directionality of the $\boldsymbol{B}$-field are crucial tracers of the physical conditions of a blazar jet.

Although the above polarization studies present compelling evidence for the directionality of the $\boldsymbol{B}$-field in blazar jets, for the purpose of modeling the emission from the jet, the field is usually assumed to be randomly oriented in the emission regions (e.g., Moderski et al. 2003; Böttcher & Reimer 2004; Sokolov et al. 2004; Joshi & Böttcher 2007; Graff et al. 2008). This leads to neglect of the effect of $\boldsymbol{B}$-field orientation on the simulated radiation, thus limiting the scope of such models in the quest to understand the time-dependent evolution of the particle population and subsequent radiation transfer in jets. Furthermore, prevailing theories require well-ordered $\boldsymbol{B}$-fields for the confinement and dynamics of the inner portion of a jet (McKinney et al. 2012). It is therefore important to compare $\boldsymbol{B}$-field structures implied by polarization observations with

physical jet models. Furthermore, it is necessary to incorporate those results into emission calculations for carrying out data fitting of observed spectral energy distributions (SEDs) and spectral variability patterns (SVPs).

Recently, various theoretical studies have been conducted to calculate HE polarization signatures (degree and angle of polarization) for blazar jets. Lyutikov et al. (2005) evaluated the impact of purely helical $\boldsymbol{B}$-fields on the polarization properties of optically thin synchrotron radiation for relativistic jets. They concluded that such fields could be responsible for the polarization properties of large-scale jets. On the other hand, Jamil & Böttcher (2012) explored the effects of partially ordered $\boldsymbol{B}$-fields and anisotropic particle distributions on the angle-dependent synchrotron and synchrotron self-Compton (SSC) radiation from relativistic jets. They pointed out that the $\boldsymbol{B}$-field orientation plays an important role in the normalization of the synchrotron spectrum, but at the same time, it could cause over- or underestimation of the $\boldsymbol{B}$-field strength. More recently, Zhang & Böttcher (2013) and Zhang et al. (2014) analyzed the expected HE polarization signatures of blazar jets due to the synchrotron and SSC mechanisms for a perfectly ordered and a helical $\boldsymbol{B}$-field, respectively. They considered an isotropic electron energy distribution and calculated the corresponding polarization signatures. Such scenarios could be related to some of the variability in the synchrotron polarization percentage and position angle observed in several blazars. Similarly, Marscher (2014) considered a turbulent ambient $\boldsymbol{B}$-field contained in a finite number of cells that cross a standing conical shock. The result is time-variable polarization with position angles that fluctuate about a mean value depending on the geometry of the shock and the line of sight.

Optical emission in blazars is usually associated with synchrotron radiation. Hence, an unprecedented bright optical state with substantially increased emission in the X-ray and IR wavelengths, such as that seen in the γ-ray blazar CTA 102 (Ciprini 2016) and candidate black hole binary system OJ 287 (Mukherjee 2017), could be a strong indicator of an ordered $\boldsymbol{B}$-field geometry, such as toroidal or helical, mixed with a disordered $\boldsymbol{B}$-field component. In addition, a simultaneous increase in the γ-ray flux could be due to an increase in the number of relativistic electrons. The synchrotron radiation observed for an electron distribution is highly concentrated perpendicular to the (aberrated) direction of the magnetic field and linearly polarized for an ordered $\boldsymbol{B}$-field. The value of $P(\%)$ is maximum for a purely ordered $\boldsymbol{B}$-field ($\sim$75%), which decreases as the disordered component of the $\boldsymbol{B}$-field increases. Thus, linear polarization observations coupled with photometric data provide direct information on the degree of order and the orientation of the $\boldsymbol{B}$-field (Gabuzda 2017). However, a comprehensive study to understand the effects of ordered and disordered components of the $\boldsymbol{B}$-field on the SEDs and SVPs of blazars is currently lacking from the literature.

Here we address some of the abovementioned limitations by extending our time-dependent MUlti-ZOne Radiation Feedback (MUZORF) leptonic jet model (Joshi et al. 2014, hereafter Paper II), which calculates the synchrotron, SSC, and external Compton (EC) emission from blazar jets. We study the impact of various geometries of the field—parallel, perpendicular, oblique, toroidal, and helical—on the time-dependent evolution of the SEDs and SVPs of a generic blazar for purely ordered field and partially ordered $\boldsymbol{B}$-field cases. The model uses internal shocks as sites of acceleration of particles to ultrarelativistic energies (Joshi & Böttcher 2011, hereafter Paper I). We assume that with the passage of shocks in the emission region, the strength of the $\boldsymbol{B}$-field gets enhanced, and the field becomes ordered. It is at this point that the geometry and strength of the modified field begin to impact the jet emission through optically thin synchrotron radiation. The modified synchrotron radiation field is further used to calculate the subsequent SSC emission. The external seed photon field required to calculate the EC component is assumed to be unpolarized.

Wentzel (1969) demonstrated that, in the case of cosmic-ray particles, the electrons get nearly isotropized in the presence of an ordered $\boldsymbol{B}$-field component as they scatter off of hydromagnetic waves present in ionized plasma. The waves get generated from electrons moving in a direction roughly parallel to the field. These plasma waves, in turn, scatter those electrons back to maintain a nearly isotropic distribution of the pitch angle with respect to the field. Thus, most relativistic electrons that are responsible for carrying most of the kinetic energy can be considered to be nearly isotropic in sources, such as radio galaxies or quasi-stellar objects. Similarly, Kardashev (1962) showed that the synchrotron energy losses and the shape of the resulting spectrum are independent of the distribution of the pitch angle in the presence of particle injection of a constant power-law spectrum. Hence, the effects of an anisotropic electron distribution in the presence of an ordered magnetic field have been ignored in this work.

In Section 2, we describe our framework of including various $\boldsymbol{B}$-field orientations in the calculation of optically thin synchrotron radiation for the cases of purely and partially ordered $\boldsymbol{B}$-fields. In Section 3, we describe our baseline model (base set) that uses a randomly oriented $\boldsymbol{B}$-field, its simulated results, and the relevant physical input parameters that we use in the study. In Section 4, we present our parameter study results and discuss the effects of varying relevant input parameters on the simulated SEDs and SVPs. We discuss the observational signatures of our findings in Section 5 and summarize in Section 6. Throughout this paper, we have used the notation $F_\nu \propto \nu^{-\alpha}$, where α is the photon energy spectral index and F_ν is the flux density. We denote quantities referring to the rest frame of the active galactic nucleus (AGN; lab frame) with *, while primed quantities refer to the comoving frame of the emitting plasma (plasma frame) and unprimed quantities refer to the observer's frame. We denote the dimensionless photon energy by $\epsilon = \frac{h\nu}{m_e c^2}$.

2. Methodology

Previous theoretical efforts have investigated the impact of the initial field topology (dipolar, quadrupolar, purely toroidal) on the launching and nature of the jet (McKinney & Gammie 2004; De Villiers et al. 2005; Beckwith et al. 2008). Observational studies of the polarization of AGN jets have supported the possibility that the characteristic behavior of the polarization is due to the presence of toroidal or helical field configurations (Gabuzda et al. 2004). An initial poloidal $\boldsymbol{B}$-field configuration threading the jet can be stretched out by velocity shear to give rise to a parallel field topology on subparsec to parsec scales. On the other hand, on such length scales, transverse or oblique fields could arise from shearing of magnetic loops threading the jet or shock compression of an initial poloidal field. In addition, compression of an already existing tangled $\boldsymbol{B}$-field by relativistic shocks in the plane of

compression perpendicular to the direction of shock flow could also give rise to a $\boldsymbol{B}$-field orthogonal to the jet (Laing 1980; Cawthorne & Wardle 1988; Hughes et al. 1989; Cawthorne & Cobb 1990). Similarly, an initial large-scale helical field threading the jet could be compressed to give rise to a toroidal field configuration, or, in a dipole topology, the radial field could be sheared to create and amplify a toroidal field (Beckwith et al. 2008). Therefore, it is important to understand the dynamic impact of various orientations of the $\boldsymbol{B}$-field on the characteristics of jet emission.

In this paper, we consider the impact of both purely ordered and disordered components of the $\boldsymbol{B}$-field on the SEDs and SVPs of a generic blazar. A fraction, $b_{\rm ord}$, of the $\boldsymbol{B}$-field is used to obtain the purely ordered component, with mean $\boldsymbol{B}$-field direction relative to the orientation of the jet axis, whereas $(1 - b_{\rm ord})$ provides the disordered component of the field. The corresponding field strengths are subsequently used together to evaluate synchrotron and SSC emissions emanating from the jet in a time-dependent manner. For the purely ordered component, the directions considered relative to the jet axis are parallel, perpendicular, oblique, toroidal, and helical.

In MUZORF, we use a colliding-shells model to invoke a collision between two shells of plasma that leads to the formation of forward and reverse shocks. The shocks accelerate particles inside a cylindrical emission region to very high energies. The energized particles then produce the observed radiation. As described in Paper I, we slice the single emission region into multiple zones and use photon escape probability functions for a cylindrical geometry to accurately evaluate the radiation transfer within each zone and in between zones. Also, we include light travel time delays to calculate the observed synchrotron, SSC, and EC radiation. In our framework, we estimate the EC emission of blazars using anisotropic radiation fields of the accretion disk, the broad-line region (BLR), and the dusty torus (DT) (Paper II). The time-dependent evolution of particle and photon populations in the emission region is followed to distances beyond the BLR and into the DT. The multizone feature of our setup lets us address the issue of inhomogeneity in the photon and electron populations throughout the emitting volume that has been neglected in other theoretical approaches (Lyutikov et al. 2005). In order to incorporate this feature, the cylindrical emission region is divided lengthwise into multiple zones. There is no division in the radial or azimuthal direction. A fraction of the total photon pool from one zone is fed into adjacent zones on either side. This feedback in forward and backward directions is the volume- and angle-averaged photon density from the radiating zone. We obtain this density by calculating a seminumerical expression for the volume- and angle-averaged photon escape density for a cylindrical geometry in three directions: forward, backward, and sideways (Paper I). The total photon pool of a zone includes synchrotron, SSC, and EC components of that zone for the current time step, along with the feedback it received from its adjacent zones in the previous time step.

2.1. Optically Thin Synchrotron Radiation

The optically thin synchrotron radiation is emitted in the same direction as the motion of the relativistic electrons. Hence, we define the pitch angle to be the angle between the magnetic field and the line of sight, corrected for relativistic aberration in the plasma frame. For a power-law distribution of electrons, the synchrotron emission coefficient, $j'_{\nu'}$, depends on the strength of the magnetic field, B', and the pitch angle, χ', according to (Rybicki & Lightman 1979)

$$j'_{\nu'} \propto (B' \sin \chi')^{1+\alpha}. \tag{1}$$

As illustrated in Papers I and II, we assume the emitting volume to be well collimated out to parsec-scale distances (see Jorstad et al. 2005) and do not consider the effects of adiabatic expansion on the evolution of the electron population or the magnetic energy density in the emission region. We do not simulate radio emission because we follow only the early phase of γ-ray production corresponding to a shock position up to $\sim$1 pc in the lab frame. During this phase, the emission region is highly optically thick to GHz radio frequencies. Hence, the calculated radio flux is well below the observed value, which is dominated by emission from more extended regions.

In order to calculate the pitch angle for various $\boldsymbol{B}$-field orientations, let us consider a single cylindrical zone of the emission region. As described in Joshi et al. (2016), where we presented the preliminary results of our study, let r, ϕ, and z be the cylindrical coordinates centered on the jet axis with corresponding plasma frame coordinates denoted by r', ϕ', and z'. The corresponding rectangular coordinates are denoted by x, y, and z. The observer's line of sight makes an angle $\theta_{\rm obs}$ with the jet axis, and we assume that the observer is located in the x–z plane so that the unit vector along the direction of emitted photons is given by $\hat{n} = (\sin\theta_{\rm obs}, 0, \cos\theta_{\rm obs})$. The emission region is assumed to be moving along the z-axis with a bulk Lorentz factor (BLF) $\Gamma_{\rm sh}$ (see Paper I for details of its evaluation). The corresponding Doppler boosting factor is given by

$$D = \frac{1}{\Gamma_{\rm sh}(1 - \beta_{\rm sh}\cos\theta_{\rm obs})}, \tag{2}$$

where $\beta_{\rm sh} = \sqrt{1 - \frac{1}{\Gamma_{\rm sh}^2}}$. We assume that the $\boldsymbol{B}$-field maintains the same (chosen) orientation throughout the emission region. The unit vector of the field, in the plasma frame, is represented by $\hat{B}'$. For the purpose of our current study, we have ignored any bulk rotation of the jet.

The primary modification to MUZORF is made through the calculation of optically thin synchrotron radiation, as explained in Equation (1). The pitch angle is calculated using $\cos\chi' = \hat{B}' \cdot \hat{n}'$. As shown in Equation (1) of Joshi et al. (2016), we can write

$$\hat{n}' = \frac{\hat{n} + \Gamma_{\rm sh}\boldsymbol{\beta}_{\rm sh}\left[\frac{\Gamma_{\rm sh}}{\Gamma_{\rm sh}+1}(\hat{n}\cdot\boldsymbol{\beta}_{\rm sh}) - 1\right]}{\Gamma_{\rm sh}(1 - \hat{n}\cdot\boldsymbol{\beta}_{\rm sh})}. \tag{3}$$

In addition to the primary modification, which is responsible for how the optically thin synchrotron radiation would be seen by an observer in the presence of an ordered magnetic field, there are two more modifications to optically thin synchrotron radiation that need to be considered when including the orientation of the magnetic field. This is important, as the inclusion of field topology leads to some effects that need to be addressed in order to correctly calculate the SSC radiation from the emission region. These effects arise because the radiation field as seen by each zone is not always the same as that seen by an observer. The first modification relates to the electrons' line of sight and how the electrons in a particular zone will perceive the optically thin synchrotron radiation in the presence of an ordered $\boldsymbol{B}$-field. In this case, each electron will see some

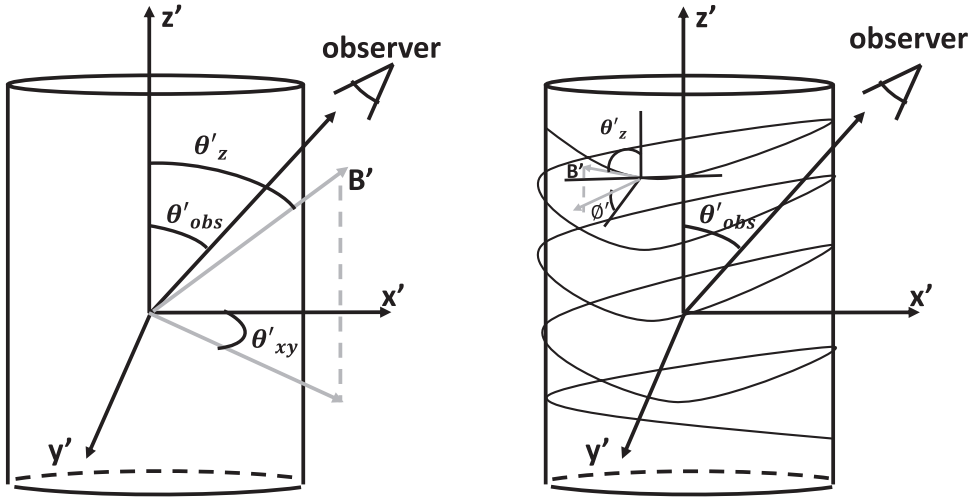

Figure 1. Schematic diagram of an oblique (left) and a helical (right) topology of the ***B***-field in a single cylindrical zone. See Section 2.2 for definitions of corresponding angles.

synchrotron photons being generated by neighboring electrons in all directions. As a result, the synchrotron radiation that will be received by that electron for upscattering will be effectively angle-averaged synchrotron radiation, regardless of the orientation of the ***B***-field. The second modification is associated with the zones' line of sight and the corresponding amount of optically thin synchrotron radiation that they will receive in the form of feedback from their adjacent zones in the presence of an ordered ***B***-field. Hence, the unit vector for the line of sight of a zone in the forward direction will be $\hat{n}'_{\rm feed\text{-}up} = (0, 0, 1)$ and in the backward direction $\hat{n}'_{\rm feed\text{-}down} = (0, 0, -1)$. We note that the calculation of SSC emission in Joshi et al. (2016) dealt with a special case in which we had assumed the viewing direction to be nearly identical to the preferred photon propagation direction for the feedback, that is, along the axis of the jet. Hence, the only synchrotron photons that the electrons would receive for Compton upscattering would be the photons distributed along the jet axis. As a result, an enhancement in the observed synchrotron flux would lead to more efficient feedback and an enhanced SSC component, along with the SSC emission becoming directly dependent on the ***B***-field topology. As shown in Figure 5 of Joshi et al. (2016), this effect is especially prominent for helical and toroidal geometries. However, that is an oversimplification of the real scenario, where the SSC emission is mostly independent of the ***B***-field topology for the reasons mentioned above. We discuss the calculation of various pitch angles that are required to incorporate the abovementioned modifications into our framework in the section below.

2.2. Purely Ordered Magnetic Field

Since parallel and perpendicular ***B***-fields are special cases of oblique fields, while toroidal geometry is a subset of a helical topology, we do not derive their corresponding pitch angles here. For the case of a purely ordered field, Figure 1 shows an oblique (left) and a helical (right) ***B***-field topology in a single cylindrical zone. For an oblique ***B***-field, $\boldsymbol{B}' = B'(\sin\theta'_{\rm z}\cos\theta'_{\rm xy}, \sin\theta'_{\rm z}\sin\theta'_{\rm xy}, \cos\theta'_{\rm z})$. Using Equation (2) of Joshi et al. (2016), we obtain

$$\hat{n}'\cdot\hat{B}' = D\{(\hat{n}\cdot\hat{B}') + \left[\frac{\Gamma_{\rm sh}^2}{\Gamma_{\rm sh}+1}(\hat{n}\cdot\boldsymbol{\beta}_{\rm sh}) - \Gamma_{\rm sh}\right](\boldsymbol{\beta}_{\rm sh}\cdot\hat{B}')\}. \quad (4)$$

Inserting expressions for $\hat{n}'$ and $\hat{B}'$ from above, we obtain the corresponding pitch angle for this case as

$$\hat{n}'\cdot\hat{B}' = \cos\chi' = D\{\sin\theta_{\rm obs}\sin\theta'_{\rm z}\cos\theta'_{\rm xy} + \Gamma_{\rm sh}\cos\theta'_{\rm z}(\cos\theta_{\rm obs} - \beta_{\rm sh})\}. \quad (5)$$

In addition, the pitch angle corresponding to the feedback that a particular zone would receive in the forward direction is

$$\cos\chi'_{\rm feed\text{-}up} = \cos\theta'_{\rm z}\,, \quad (6)$$

which gives us

$$\sin\chi'_{\rm feed\text{-}up} = \sqrt{1-\cos^2\theta'_{\rm z}} = \sin\chi'_{\rm feed\text{-}down}\,. \quad (7)$$

By virtue of the geometry of the emission region, the pitch angle for the backward-direction feedback will be the same as that of the forward direction for all cases considered here. From Equation (5), it can be seen that the sine of the pitch angle for a parallel orientation can be obtained for a value of $\theta'_{\rm z} = 0°$ and that for a perpendicular field for $\theta'_{\rm z} = 90°$. On the other hand, the sine of the pitch angle for feedback for a parallel geometry would be zero, whereas that for a perpendicular orientation would be 1.

In Figures 2 and 3, we show the impact of varying $\Gamma_{\rm sh}$, $\theta_{\rm obs}$, $\theta'_{\rm xy}$, and $\theta'_{\rm z}$ on $\sin\chi'$ for the case of an oblique geometry. As can be seen from the top left panel of Figure 2, the pitch angle becomes nearly zero for that combination of $\Gamma_{\rm sh}$ and $\theta_{\rm obs}$ for which relativistic aberration results in $\sin\chi' \sim 0$. This implies that when the jet is viewed nearly face-on and happens to have a higher BLF, the synchrotron emission can become nearly zero in the presence of an oblique ***B***-field. Similarly, the bottom right panel of Figure 2 shows the combination of $\theta'_{\rm xy}$, $\theta'_{\rm z}$, and $\Gamma_{\rm sh}$ leading to a very low value of $\sin\chi'$ when such a jet is viewed at a larger viewing angle. For the rest of the combinations of these parameters, the value of $\sin\chi'$ essentially

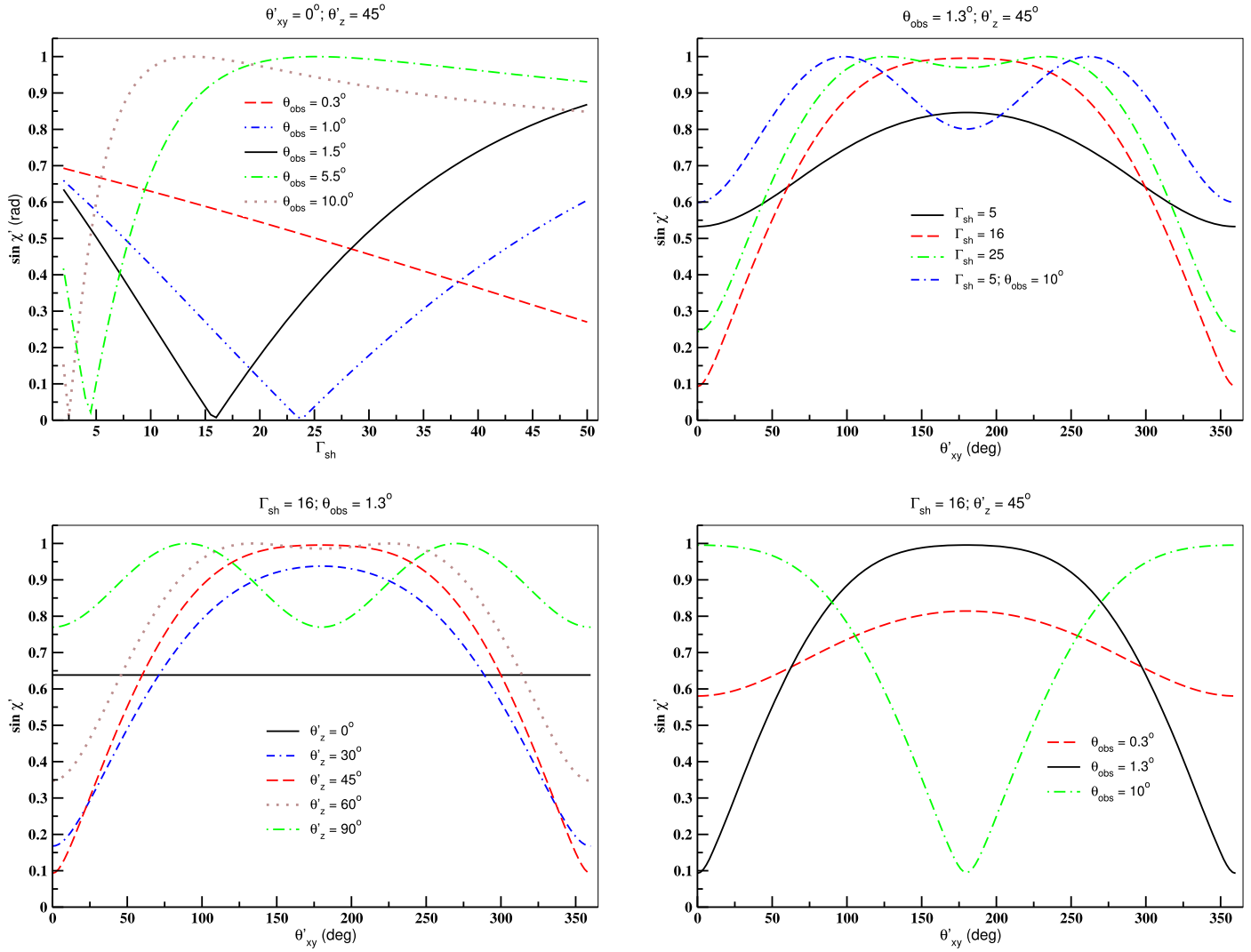

Figure 2. Panels showing the dependence of the pitch angle, $\sin\chi'$, on the variation of $\Gamma_{\rm sh}$ (top left) for various values of $\theta_{\rm obs}$, $\theta'_{\rm xy}$ (top right) for various values of $\Gamma_{\rm sh}$, $\theta'_{\rm xy}$ (bottom left) for various values of $\theta'_{\rm z}$, and $\theta'_{\rm xy}$ (bottom right) for various values of $\theta_{\rm obs}$ while keeping the remaining two parameters constant, as indicated in the graphs' subtitles.

follows the cosine dependence of $\theta'_{\rm xy}$, as is evident from Equation (5). The same sinusoidal dependence is also demonstrated by the pitch angle in Figure 3 for a variation in $\theta_{\rm ob}$ and $\theta'_{\rm z}$.

Now, considering a helical field threading the emission region such that the poloidal component of the field makes an angle $\theta'_{\rm z}$ with the jet axis, the $\boldsymbol{B}$-field is given by (Lyutikov et al. 2005)

$$\boldsymbol{B}' = B'_{\phi}\hat{\phi}' + B'_{z}\hat{z}' = B'\sin\theta'_{\rm z}(-\sin\phi')\hat{x}' + B'\sin\theta'_{\rm z}\cos\phi'\hat{y}' + B'\cos\theta'_{\rm z}\hat{z}'. \quad (8)$$

Following Equation (2) of Joshi et al. (2016), we obtain

$$\hat{n}'\cdot\hat{B}' = D\left\{-\sin\theta'_{\rm z}\sin\phi'\sin\theta_{\rm obs} + \cos\theta'_{\rm z}\cos\theta_{\rm obs} + \left[\frac{\Gamma_{\rm sh}^2}{\Gamma_{\rm sh}+1}(\beta_{\rm sh}\cos\theta_{\rm obs}) - \Gamma_{\rm sh}\right](\beta_{\rm sh}\cos\theta'_{\rm z})\right\}, \quad (9)$$

which gives

$$\hat{n}'\cdot\hat{B}' = \cos\chi' = D[\Gamma_{\rm sh}\cos\theta'_{\rm z}(\cos\theta_{\rm obs} - \beta_{\rm sh}) - \sin\theta_{\rm obs}\sin\phi'\sin\theta'_{\rm z}]. \quad (10)$$

Hence, the pitch angle for a helical topology in the plasma frame is

$$\sin\chi' = \sqrt{1 - D^2[\Gamma_{\rm sh}\cos\theta'_{\rm z}(\cos\theta_{\rm obs} - \beta_{\rm sh}) - \sin\theta_{\rm obs}\sin\phi'\sin\theta'_{\rm z}]^2}\,. \quad (11)$$

As far as the feedback is concerned, similar to the oblique geometry case, the corresponding pitch angle is

$$\cos\chi'_{\rm feed\text{-}up} = \cos\theta'_{\rm z}\,, \quad (12)$$

which gives us

$$\sin\chi'_{\rm feed\text{-}up} = \sqrt{1-\cos^2\theta'_{\rm z}} = \sin\chi'_{\rm feed\text{-}down}\,. \quad (13)$$

The variable ϕ' represents the azimuthal angle of the loop of a toroidal or helical magnetic field. In our current framework,

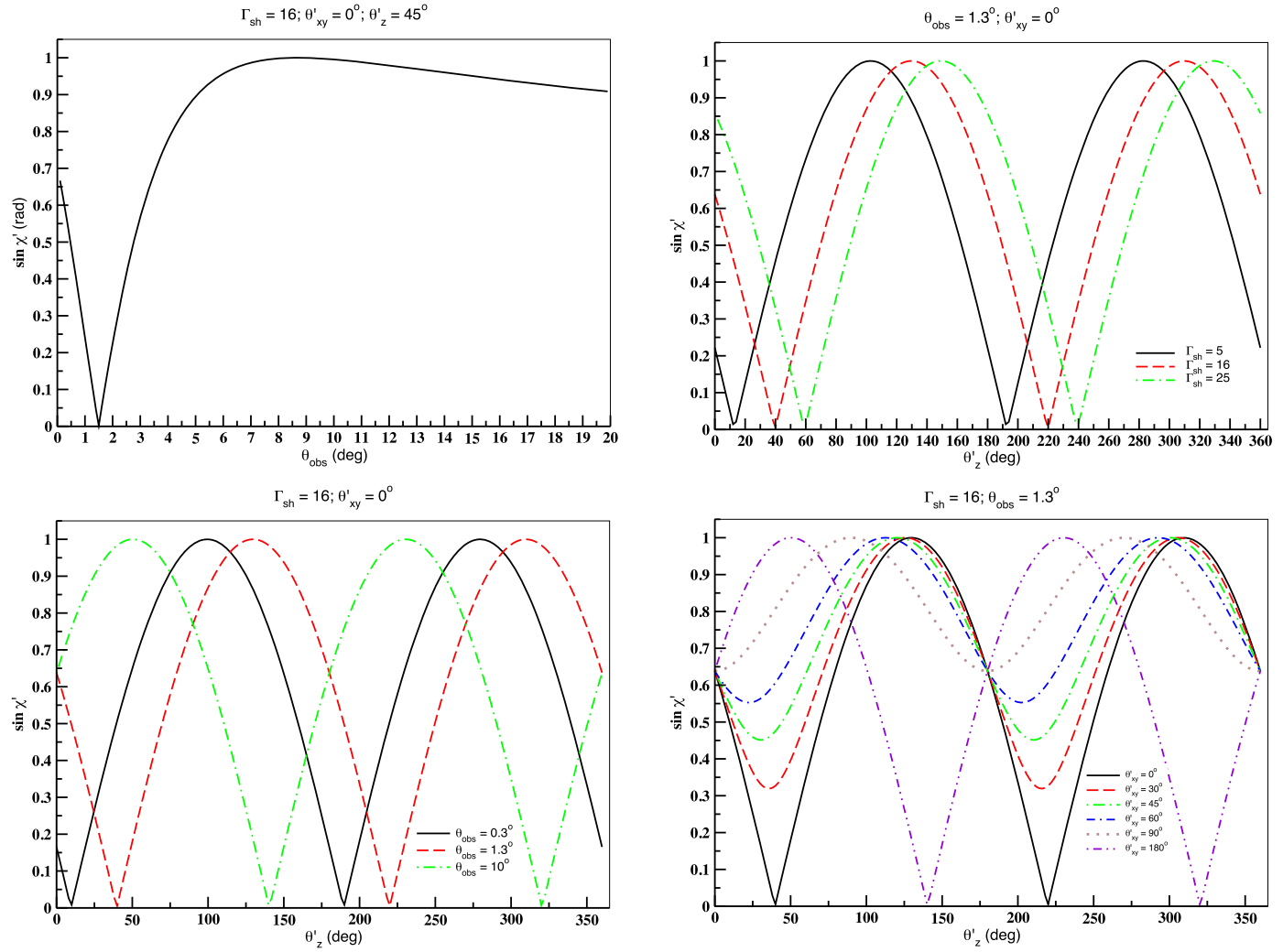

Figure 3. Panels exhibiting the profile of the pitch angle, $\sin\chi'$, as a function of $\theta_{\rm obs}$ (top left), $\theta'_{\rm z}$ (top right) for various values of $\Gamma_{\rm sh}$, $\theta'_{\rm z}$ (bottom left) for various values of $\theta_{\rm obs}$, and $\theta'_{\rm z}$ (bottom right) for various values of $\theta'_{\rm xy}$ while keeping the other parameters the same, as indicated in the graphs' subtitles.

we represent the loop of such fields by eight azimuthal angles ranging from 0° to 315° in increments of 45°. For each azimuthal angle, we calculate the $\sin\chi'$ that the plasma frame line of sight makes with the magnetic field component directed along that ϕ'. We calculate synchrotron radiation along each of these directions and then add them together to obtain the final synchrotron radiation resulting from such a geometry.

Using Equation (10), it can be seen that the pitch angle for a toroidal field can be obtained for a value of $\theta'_{\rm z} = 90°$. Similar to the perpendicular case, the sine of the pitch angle for the feedback for a toroidal geometry would be 1.

The quantities that are affected by the inclusion of $\boldsymbol{B}$-field orientation are synchrotron emissivity, synchrotron self-absorption (SSA) optical depth, and SSC emissivity. The synchrotron photon production rate per unit volume in the photon energy interval $[\epsilon,\ \epsilon + d\epsilon]$ is calculated according to the formula

$$\dot{n}'_{\rm syn}(\epsilon',\chi') = \frac{\sqrt{3}\,e^3 B'\sin\chi'}{4\pi h^2\nu}\int_1^\infty F(x) n_{\rm e}(\gamma)' d\gamma' \,, \qquad (14)$$

where $x = \frac{4\pi m_e c\nu'}{3eB\gamma'^2\sin\chi'}$ and $F(x)$ is as defined in Rybicki & Lightman (1979). In order to save computation time, we have obtained a numerically simplified approximation of the function $F(x)$ as

$$F(x) = (A_1 x^{b_1} - A_2 x^{b_2}) e^{-x} \,, \qquad (15)$$

where $A_1 = 1.77205$, $A_2 = 6.51657\times10^{-4}$, $b_1 = 0.29363$, and $b_2 = 0.50372$. Figure 4 compares the synchrotron spectrum calculated using the exact expression with the approximation in the range $10^{-2} < x < 10$. As can be seen, the approximation is accurate to better than 1% in this range.

In order to incorporate the effects of SSA on the synchrotron spectrum under our current formalism, we calculate the SSA optical depth according to

$$\tau'_{\rm SSA}(\chi') = \frac{-l'_{\rm ph,esc}\sqrt{3}\,e^3}{8\pi^2(m_{\rm e}c)^2}\frac{B'\sin\chi'}{\nu'^2}\int_1^\infty F(x)\gamma'^2 \times \frac{d}{d\gamma'}\left(\frac{n'_{\rm e}(\gamma')}{\gamma'^2}\right)d\gamma' \,, \qquad (16)$$

where $l'_{\rm ph,esc} = t'_{\rm ph,esc}\,c$ is the mean path length traversed by a photon escaping from its point of origin inside a cylindrical region. The synchrotron emission from a cylindrical region is then obtained using the expression given in Equation (33) of Paper I.

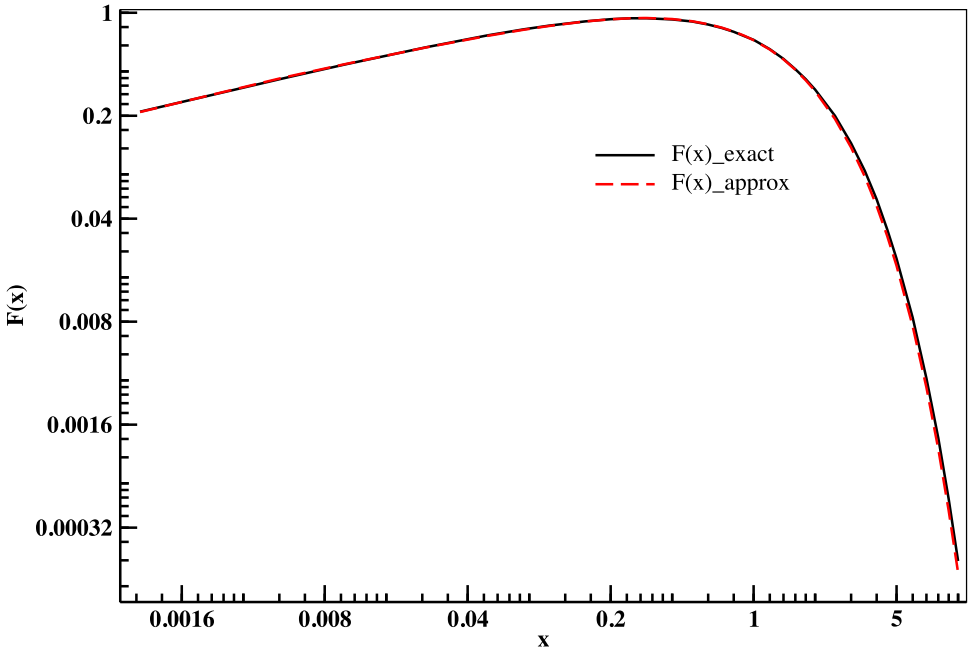

Figure 4. Comparison of the exact ($F(x)_{\rm exact}$) expression and numerical approximation ($F(x)_{\rm approx}$) of $F(x)$. The fit is accurate to ∼0.5% in the range $10^{-2} < x < 10$.

2.3. Disordered Magnetic Field Component

In order to incorporate the effects of a partially ordered field into our framework, we need to account for its fraction responsible for shaping the synchrotron spectrum. The total spectral synchrotron power radiated at position r and frequency ν' is given by Crusius & Schlickeiser (1986),

$$P'_{\rm total}(\nu',\,\chi') = b_{\rm ord}\,P'_{\rm h}(\nu',\,\chi') + (1-b_{\rm ord})\,P'_{\rm r}(\nu')\,, \quad (17)$$

where $P'_{\rm h}$ and $P'_{\rm r}$ are homogeneous and random spectral powers, respectively; $b_{\rm ord} = 0$ refers to a completely randomly oriented field; and $b_{\rm ord} = 1$ implies a purely ordered $\boldsymbol{B}$-field.

Hence, the corresponding photon production rate is obtained using

$$\dot{n}'_{\rm tot}(\epsilon',\,\chi') = b_{\rm ord}\,\dot{n}'_{\rm syn}(\epsilon',\,\chi') + (1-b_{\rm ord})\,\dot{n}'_{\rm syn}(\epsilon')\,, \quad (18)$$

where $\dot{n}'_{\rm syn}(\epsilon',\,\chi')$ (see Equation (14)) and $\dot{n}'_{\rm syn}(\epsilon')$ (see Equation (31) of Paper I) are the photon production rates of a purely ordered and randomly oriented $\boldsymbol{B}$-field, respectively.

The SSA optical depth under such a scenario can be obtained using

$$\tau'_{\rm SSA,tot}(\chi') = b_{\rm ord}\,\tau'_{\rm SSA}(\chi') + (1-b_{\rm ord})\,\tau'_{\rm SSA}\,, \quad (19)$$

where $\tau'_{\rm SSA}(\chi')$ (see Equation (16)) and $\tau'_{\rm SSA}$ (see Equation (32) of Paper I) are SSA optical depths for a purely ordered and randomly oriented field, respectively.

The final synchrotron spectrum, observed in the presence of purely and partially ordered $\boldsymbol{B}$-fields, is calculated using Equations (18) and (19). We calculate the SSC emissivity and energy-loss rate according to the method described in Paper I. However, the radiation field that is now available for SSC scattering includes the modified synchrotron emissivity. As explained in Section 2.1, the SSC emission for a particular zone is calculated using the angle-averaged synchrotron radiation for that zone to account for electrons' lines of sight and the anisotropic synchrotron field (to account for the zone's line of sight) that the zone receives in the form of feedback from its adjacent zones. Here we point out that the formula given in Paper I for calculating SSC emission involves an isotropic seed photon field. However, in the current scenario, the synchrotron radiation is anisotropic. Despite this, we can ignore the effects of the Compton emissivity scaling factor $(1-\beta\mu)$ (where μ is the cosine of the angle between the line of sight and the incoming photon direction), as they are considered to be quite small in comparison to the effects of an angle-averaged distribution of synchrotron photons getting upscattered to produce SSC emission. In addition, we do not consider any transfer of radiation among different azimuthal slices for toroidal or helical geometries. This is justified because, as explained above, we consider angle-averaged synchrotron radiation of the zone to calculate the corresponding SSC emission. Hence, any angle dependence of the synchrotron radiation emanating from individual azimuthal slices can be ignored in the treatment of SSC emission from a particular zone.

3. Parameter Study

We explore the combined effects of purely and partially ordered $\boldsymbol{B}$-fields for various field topologies on the jet emission of a generic blazar by studying the impact of varying relevant input parameters on the time-dependent evolution of its SEDs and SVPs.

3.1. Our Baseline Model

In this study, the flux values are calculated for a frequency range of $\nu' = (7.5\times10^{8}$–$7.5\times10^{24})$ Hz and an electron energy distribution ranging over $\gamma' = 10$–10^{8}. The code setup is as described in Paper II. Table 1 delineates the values of the input parameters used to build our baseline model (run 1) for conducting the parameter study. The parameters of this generic blazar are motivated by a fit to the blazar 3C 454.3 for modeling rapid variability on a timescale of ∼1 day. The input parameters were previously explained in Papers I and II, except for $\theta'_{\rm xy}$, $\theta'_{\rm z}$, *Orientation*, and $b_{\rm ord}$. The quantity $\theta'_{\rm xy}$ refers to the

Table 1
Parameter List of Run 1 Used to Obtain the Baseline Model

Parameter	Symbol	Value
Kinetic luminosity	L_w^*	1×10^{48} erg s^{-1}
Event duration	t_w^*	1.8×10^7 s
Outer shell mass	M_o^*	5.38×10^{32} g
Inner shell BLF	Γ_i^*	26
Outer shell BLF	$\Gamma^*{}_o$	11
Inner shell width	Δ_i^*	5.7×10^{15} cm
Outer shell width	Δ_o^*	8.3×10^{15} cm
Inner shell position	z_i^*	7.8×10^{15} cm
Outer shell position	z_o^*	1.65×10^{16} cm
Electron energy partition parameter	ε_e'	0.3
Magnetic energy partition parameter	ε_B'	1×10^{-4}
Fraction of accelerated electrons	ζ_e'	2.5×10^{-2}
Acceleration timescale parameter	α'	1×10^{-6}
Particle injection index	q'	4.0
Slice/jet radius	R_z'	3.43×10^{16} cm
Observer frame observing angle	$\theta_{\rm obs}$	1°.3
Disk luminosity	$L_{\rm disk}^*$	2×10^{46} erg s^{-1}
Black hole mass	$M_{\rm BH}^*$	$1 \times 10^9 M_\odot$
Accretion efficiency	$\eta_{\rm acc}$	0.1
BLR luminosity	$L_{\rm BLR}^*$	8×10^{44} erg s^{-1}
BLR inner radius	$R_{\rm in,BLR}^*$	6.17×10^{17} cm
BLR outer radius	$R_{\rm out,BLR}^*$	1.85×10^{18} cm
BLR optical depth	$\tau_{\rm BLR}$	0.01
BLR covering factor	$f_{\rm cov,BLR}$	0.03
DT inner radius	$R_{\rm in,DT}^*$	3.086×10^{18} cm
DT outer radius	$R_{\rm out,DT}^*$	8.994×10^{18} cm
Ldisk fraction	ξ	0.2
DT covering factor	$f_{\rm cov,DT}$	0.2
Redshift	z	0.859
Angle in x'–y' plane	$\theta_{\rm xy}'$	0°
Angle with z'-axis	$\theta_{\rm z}'$	0°
***B*-field**	*Orientation*	Tangled
Ordered component	$b_{\rm ord}$	0

angle that the ***B***-field makes in the x'–y' plane, whereas $\theta_{\rm z}'$ is the angle that the field makes with the z'-axis. The quantity *Orientation* refers to various field geometries—parallel, perpendicular, oblique, toroidal, and helical orientation—that have been considered in this study. The quantity $b_{\rm ord}$ refers to the fraction of the ordered component of the field that has been considered for the generic blazar. In the case of our baseline model, a completely tangled ***B***-field has been assumed to pervade the entire emission region.

The choice of our input parameters, as listed in Table 1, results in $\Gamma_{\rm sh} = 16$ and $B' = 1.43$ G for the emission region. The maximum and minimum energy cutoffs for the electron population in forward and reverse emission regions are $\gamma'_{\rm max} = 4 \times 10^4$, $\gamma'_{\rm min,fs} \sim 1000$, and $\gamma'_{\rm min,rs} \sim 2000$, respectively. The total width of the emission region is obtained to be $\Delta'_{\rm cyl} = 3.2 \times 10^{16}$ cm with shock-crossing times for forward and reverse emission regions of $t'_{\rm cr,fs} = 1.1 \times 10^6$ and $t'_{\rm cr,rs} = 1.4 \times 10^6$ s (Joshi et al. 2016). In the observer's frame, this translates into the forward shock leaving its emission region in ∼20 hr and the reverse shock leaving the reverse emission region in ∼26 hr. We set the width of the emission region such that the shock-crossing times of both shocks are similar to the variability timescale of our simulations, which is chosen to be around 1 day. We point out that multiwavelength outbursts of blazars typically last for ∼10 days or more. Our code, MUZORF, is completely scalable to simulate such durations. However, for the purpose of our parameter study, we choose to reproduce a flare lasting for about 1 day.

For the case of the generic blazar, the inner and outer shells collide at a distance of $z_{\rm c}^* = 1.2 \times 10^{17}$ cm, which puts the emission region in the cavity of the BLR at the start of the simulation. The entire simulation covers a time range of ∼2 days in the observer's frame, during which the emission region moves from the cavity of the BLR to within the BLR, covering a total distance of ∼0.46 pc in the AGN frame. Figure 5 shows the simulated time-averaged SED and light-curve profiles of the baseline model, where the SED and light curves have been evaluated over a time period of ∼24 hr. In the figure, the left panel illustrates the total time-averaged SED and the respective time-averaged contribution of all radiative components (synchrotron; SSC; EC due to the disk (ECD), BLR (ECBLR), and DT (ECDT); forward feedback (Feed-Up); and backward feedback (Feed-Do)) that are responsible for producing the simulated emission. As can be seen, the low-energy component of our baseline model (run 1) is governed by the synchrotron process that peaks at $\sim 10^{14}$ Hz. The turnover from synchrotron to SSC takes place in the X-rays at $\sim 3 \times 10^{16}$ Hz. The ECDT component dominates up to $\sim 10^{23}$ Hz in the γ-rays, beyond which the HE profile is governed by the ECBLR component. For the choice of input parameters considered in this study, the ECD component does not play a dominant role. The Compton dominance (CD) is indicated in terms of the Compton dominance factor (CDF), which is defined as $\mathrm{CDF} = \nu F_\nu^{\rm Compton,peak} / \nu F_\nu^{\rm syn,peak}$ and derived to be ∼143 for this case. The spectral hardness (SH) of the resultant time-averaged spectrum is determined using α. In the X-ray range of 2–10 keV, $\alpha_{\rm 2-10\ keV}$ is found to be ∼0.4, which is indicative of a hard SSC-dominated X-ray spectrum. On the other hand, in the Fermi range of 5–10 GeV, a softer γ-ray spectrum is obtained with $\alpha_{\rm 9-12\ GeV} = 2.71$.

The right side of Figure 5 shows the profiles of flares corresponding to a period of ∼24 hr for various energy bands: optical (R band), UV, X-ray (10 keV), γ-rays (1 MeV and 1 GeV), and HE γ-ray in the upper Fermi range (10 GeV) for our baseline model. The choice of energy bands at which light curves are calculated in this study is based on the frequencies at which observations of blazars are typically carried out in various telescopes operating in the optical–to–γ-ray energy regime with good spectral resolution. As can be seen from the figure, the synchrotron-dominated optical/UV and EC-dominated HE flares are all governed by the presence of both shocks in the system. Since these flares involve higher-energy electrons, which lose energy on a timescale shorter than the dynamical timescale of a zone, corresponding pulses rise steadily for as long as particle acceleration is active in both emission regions (see Papers I and II). As a result, the corresponding R and UV bands and 10 GeV pulses start to decay as soon as radiative cooling starts to dominate over particle acceleration once one of the shocks exits the system. For these energy bands, the pulse reaches its maximum at $t_{\rm peak} \sim 6300$ s or 17.5 hr, after which they rapidly decline. In the case of 10 keV and 1 MeV energies, the corresponding pulses are dominated by SSC and SSC+ECDT processes, respectively, whereas the 1 GeV pulse is a result of the ECBLR process with some contribution from the ECDT component. Generation of such photons involves lower-energy electrons.

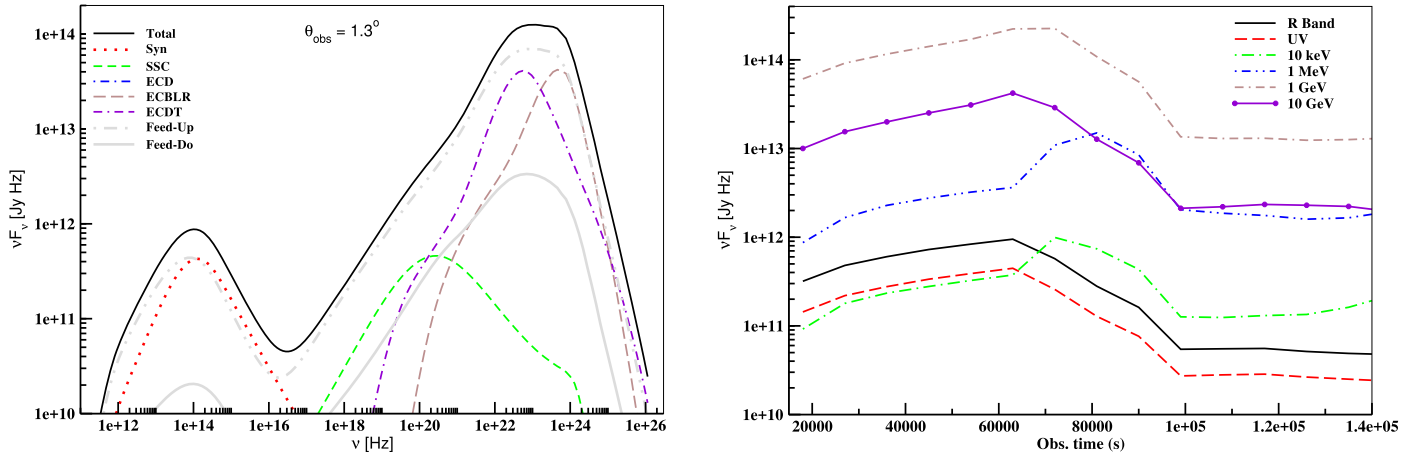

Figure 5. Left: time-averaged SED of the generic blazar, shown by a black solid line, averaged over a period of ∼24 hr (Joshi et al. 2016). The contribution of various radiative components is indicated by lines shown as dotted: synchrotron; small-dashed: SSC; dotted–dashed: ECD (not visible, as its flux level is $<10^{10}$ Jy Hz for this case); long-dashed: ECBLR; dotted–double-dashed: ECDT; dashed–double-dotted: Feed-Up; thick solid with circles: Feed-Do. Right: corresponding light curves of the blazar calculated for the *R* and UV bands and at photon energies of 10 keV, 1 MeV, 1 GeV, and 10 GeV. The plot is shown on a linear-log scale.

Table 2
Parameter List for Simulations Illustrating the Effect of Varying Intrinsic Parameters Relevant for Magnetic Field Orientation

Orientation	Run No.	$\theta_{\rm obs}$	$\theta'_{\rm xy}$	$\theta'_{\rm z}$	$\sin\chi'$	$\sin\chi'_{\rm feed}$
Oblique	2a	1.°3	0°	45°	9.30×10^{-2}	0.71
	2b	1.°3	30°	45°	3.54×10^{-1}	
	2c	1.°3	45°	45°	5.04×10^{-1}	
	2d	1.°3	60°	45°	6.38×10^{-1}	
	2e	1.°3	90°	45°	8.39×10^{-1}	
	2f	1.°3	120°	45°	9.48×10^{-1}	
	2g	1.°3	150°	45°	9.88×10^{-1}	
	2h	1.°3	180°	45°	9.96×10^{-1}	
	2i	1.°3	0°	39.°66	6.01×10^{-7}	0.64
	2j	1.°3	45°	39.°66	4.74×10^{-1}	
	2k	1.°3	90°	39.°66	8.05×10^{-1}	
Helical	3a	1.°3	⋯	30°	$\phi'=0°$: 0.745	0.5
					$\phi'=45°$: 0.897	
					$\phi'=90°$: 0.938	
					$\phi'=135°$: 0.897	
					$\phi'=180°$: 0.745	
					$\phi'=225°$: 0.451	
					$\phi'=270°$: 0.168	
	3b	1.°3	⋯	45°	$\phi'=0°$: 0.839	0.71
					$\phi'=45°$: 0.974	
					$\phi'=90°$: 0.996	
					$\phi'=135°$: 0.974	
					$\phi'=180°$: 0.839	
					$\phi'=225°$: 0.504	
					$\phi'=270°$: 0.093	
	3c	1.°3	⋯	60°	$\phi'=0°$: 0.923	0.87
					$\phi'=45°$: 0.99998	
					$\phi'=90°$: 0.986	
					$\phi'=135°$: 0.99998	
					$\phi'=180°$: 0.923	
					$\phi'=225°$: 0.631	
					$\phi'=270°$: 0.348	

As explained in Papers I and II, such electrons take time to accumulate and stay in the system for a much longer period of time. Hence, they peak later compared to their optical/UV and HE γ-ray counterparts and take longer to decay, which makes their profiles asymmetric.

For the rest of the cases considered below, we only show pulse profiles that are different from their run 1 counterparts. Hence, we mostly limit our discussion on the impact of purely and partially ordered ***B***-fields to the *R*, 10 keV, 1 MeV, and 1 GeV energy bands only.

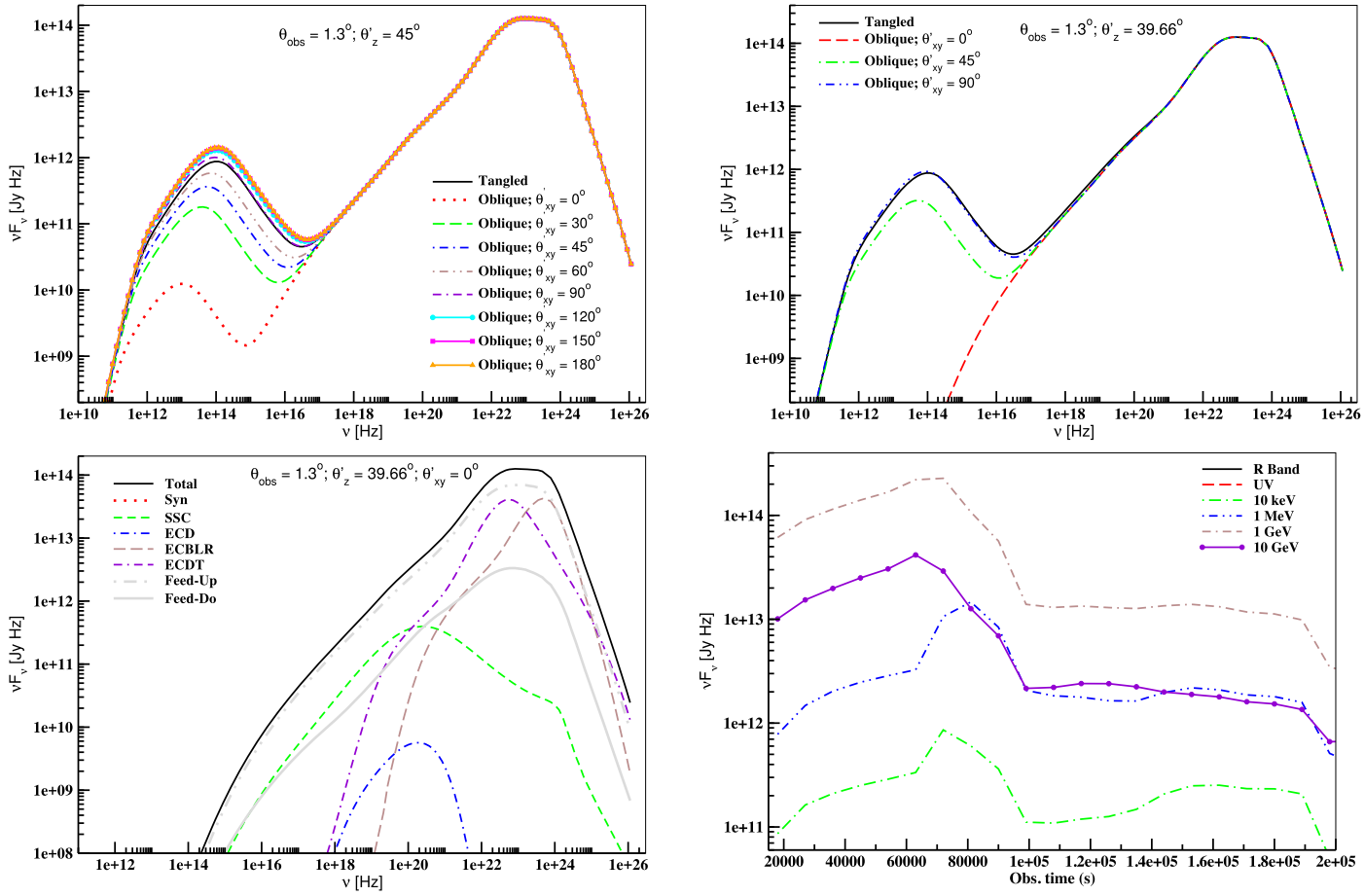

Figure 6. Top left: comparison of time-averaged SEDs of a blazar for purely oblique (runs 2a–2h) and tangled (run 1) ***B***-fields. For the oblique geometry, the SEDs are generated by varying θ'_{xy} from 0° to 180° while keeping θ'_z constant at 45°, as indicated in the graph legends. Top right: comparison of time-averaged SEDs for runs 2i–2k and 1. For these cases, the SEDs are generated by varying θ'_{xy} from 0° to 90° while keeping θ'_z constant at 39.°66. Bottom left: contributions of various radiative components responsible for generating the time-averaged SED of run 2i with $\theta'_{xy} = 0°$ and $\theta'_z = 39.°66$. Their corresponding line patterns are the same as described in Figure 5. Bottom right: corresponding light curves for run 2i calculated for the *R* and UV bands and at photon energies of 10 keV, 1 MeV, 1 GeV, and 10 GeV. The plot is shown on a linear-log scale.

3.2. Intrinsic Parameters

In order to assess the combined impact of various ***B***-field orientations and disordered ***B***-field components on the evolution of broadband spectra and light curves of blazars, we have explored the effects of varying the relevant physical parameters, i.e., θ'_{xy} and θ'_z. Since the parameters of the generic blazar mimic those of the blazar 3C 454.3, b_{ord} has been assumed to be 0.2, which is the typical value of *P*, for this blazar (Gupta et al. 2017). For all cases described below, the simulation time is the same as that of the baseline model, which is ∼2 days, while the time-averaged SEDs are obtained over a period of ∼1 day in the observer's frame. Also, the shock-crossing times are the same as that of the baseline model. Table 2 shows the values of parameters that are varied in the rest of the simulations for the case of a purely ordered ***B***-field. The impact of varying these parameters on time-averaged SEDs and light curves, with respect to that of the baseline model, is described in Sections 4.1–4.2. For the case of a purely ordered ***B***-field, we have considered only those combinations of angles that result in different values of sin χ'. In Table 2, we show a sample of such combinations for oblique and helical geometries.

In Table 2, $\theta'_z = 39.°66$ represents the viewing angle corresponding to a value of 1.°3 (considered here) in the plasma frame. This implies that at this angle, the ***B***-field is pointing toward the observer, which will result in the cancellation of any synchrotron radiation for the observer but will produce SSC emission in that direction.

4. Results

In this section, we discuss the impact of purely ($b_{ord} = 1$) oblique and helical fields by varying θ'_{xy} and θ'_z (see Figure 1) on the SEDs and SVPs of a generic blazar. Since parallel and perpendicular (including toroidal) fields are special cases of an oblique (helical) topology, we do not discuss their impacts individually but briefly summarize them in the sections below. We also compare these results with those for partially ordered fields by considering $b_{ord} = 0.2$. The impact of the disordered component on the SEDs and SVPs can be gauged from these simulated results and holds true for other combinations of angles as well. For the input parameters considered here, the superluminal cone for a generic blazar source with a BLF of 16 spreads over a half angle of $\theta_{SL} = \arcsin(1/\Gamma_{sh}) = 3.°58$. All angles considered here are within this superluminal limit.

4.1. Variation of θ'_{xy} and θ'_z

For the case of a purely oblique ***B***-field, Figure 6 shows the impact of varying θ'_{xy} for the same θ_{obs} as that of the base set

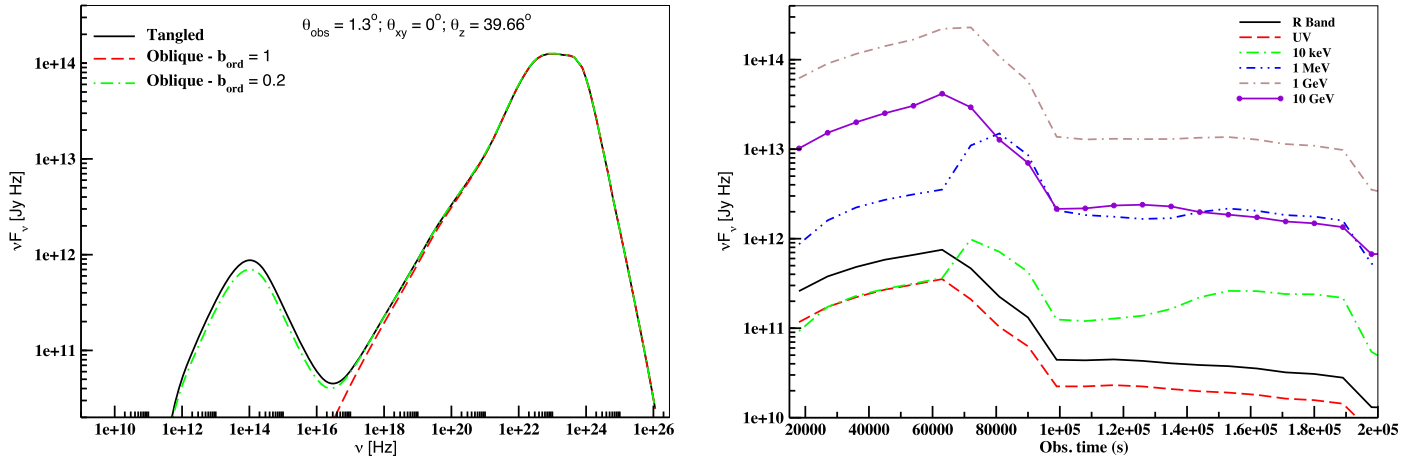

Figure 7. Left: comparison of time-averaged SEDs of a blazar for a purely oblique field (run 2i; $b_{\rm ord} = 1$) with the disordered component included (run 2i; $b_{\rm ord} = 0.2$) and tangled (run 1) ***B***-fields. Right: corresponding light curves for run 2i, with the disordered component included, calculated for the *R* and UV bands and at photon energies of 10 keV, 1 MeV, 1 GeV, and 10 GeV. The plot is shown on a linear-log scale. Compared to run 1, the overall flare profiles are exactly the same, but the flux levels of the synchrotron-dominated flares (*R* and UV bands) are slightly lower.

(run 1) while keeping θ'_z at 45° for runs 2a–2h and 39.°66 for runs 2i–2k. (Note: A value of $\theta'_z = 90°$ reproduces the case of a perpendicular magnetic field.)

As can be seen from the figure, the obliquity of the ***B***-field with respect to the z'-axis can lead to a scenario where the synchrotron flux is substantially lower (run 2a) or completely absent (run 2i) compared to its run 1 counterpart. For the set of input parameters considered here, such a situation arises for a combination of $\theta'_{xy} = 0°$ and $\theta'_z = 45°$, where the synchrotron emission declines significantly while the SSC component increases and begins to make a contribution to the previously synchrotron-dominated portion of the SED profile. As expected, the EC emission stays nearly the same. This results in a value of the CDF that is one of the largest among all cases considered for our study. As the obliquity of the field increases, the distribution of synchrotron peak frequencies among different cases decreases and converges for higher values of θ'_z, such as 120° and 150°. For these values, the overall profile of SEDs becomes similar to that of the perpendicular field case. This is expected because as θ'_z increases in value, say, varying from 30° to 150°—implying that in the observer's frame, it changes from ∼0.°96 to ∼13°—the field becomes more transverse in the comoving frame of the plasma, thereby almost reproducing the case of a perpendicular geometry.

Another extreme case is unfolded for $\theta'_z = 39.°66$. This is the value of the viewing angle in the plasma frame. As noted in Section 3.2, under this scenario, the ***B***-field is perfectly aligned with the observer's line of sight. As a result, the synchrotron emission is completely suppressed for the observer. However, the electrons continue to receive that emission and upscatter a portion of it to produce SSC radiation. Hence, the SSC emission is observable, while the synchrotron is not (see Figure 6). As shown in Table 2, the value of $\sin\chi'_{\rm feed}$ changes according to θ'_z. Hence, the corresponding SSC flux level gets impacted slightly by the variation. The locations of $\nu^{\rm peak}_{\rm syn}$ and $\nu_{\rm cutoff}$ shift to lower frequencies due to weaker synchrotron emission because of smaller values of $\sin\chi'$. The CDF is the largest for $\theta'_{xy} = 0°$ and $\theta'_z = 39.°66$, and the SH of the X-ray range is affected only very slightly, depending on the combination of θ'_{xy} and θ'_z, while that of the Fermi range is not affected at all by this geometry.

Figure 6 also shows the dependence of the light-curve profiles on the combination of $\theta'_{xy} = 0°$ and $\theta'_z = 39.°66$. The pulse profiles at all energies, for the rest of the combinations, follow similar patterns as that of run 1 and are not discussed here. As shown in the figure, the profiles of X-ray and HE γ-ray pulses are similar to those of the base set, including the overall flux level. However, both synchrotron-dominated pulses (optical and UV) are completely absent from the figure for the reasons stated above.

On the other hand, once the presence of the disordered component is taken into account, the impact of a purely ordered ***B***-field gets diluted. As an example, Figure 7 shows the comparison of the impact on the SED and SVPs of the generic blazar from run 2i for a purely oblique field ($b_{\rm ord} = 1$) and after including a disordered ***B***-field component ($b_{\rm ord} = 0.2$). As expected, the overall profiles of the SED and SVPs of the blazar are similar to that of run 1 for the case of a disordered component, since the strength of the ordered ***B***-field component has been reduced to 20%. The synchrotron flux level, however, is impacted slightly due to the mix of ordered and disordered components of the ***B***-field. As a result, it does not vanish, as in the case of a purely oblique field, but at the same time is slightly lower compared to its run 1 counterpart.

For a parallel geometry, the value of $\sin\chi'$ is guided by the sine of the viewing angle (see Equation (5) for a value of $\theta'_z = 0°$). Hence, as the viewing angle becomes smaller and our line of sight becomes aligned closer to the jet axis, the value of $\sin\chi'$ decreases. As a result, the synchrotron emission along our line of sight reduces for a smaller viewing angle. However, the HE component of the SED, which is governed by SSC and EC emissions, continues to be Doppler boosted in our direction. But in the case of SSC emission, the contribution due to radiation feedback from adjacent zones reduces to zero (see Equation (7)). Hence, the SSC flux for the parallel case turns out to be lower compared to its run 1 counterpart. The SH of the X-ray band in the 2–10 keV range increases slightly due to an increased contribution from the SSC component. The light-curve profiles at various energy bands closely follow those of the base set when the viewing angle is kept the same. However, an increase or decrease in the viewing angle shifts the time of peaking of flares across all energy bands. For a smaller value of the viewing angle, flare profiles at all energy

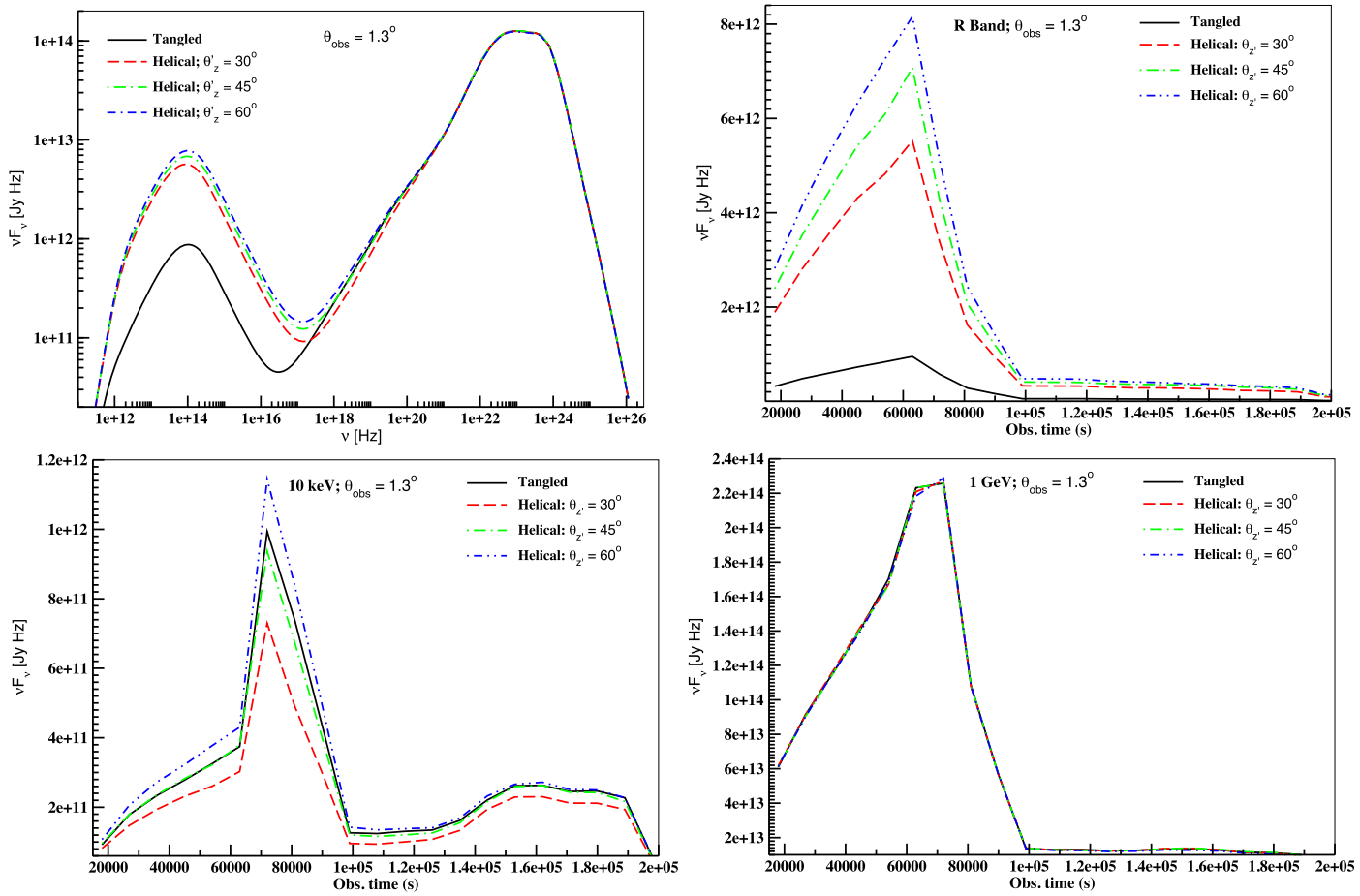

Figure 8. Top left: comparison of the time-averaged SEDs of a blazar for helical (runs 3a–3c) and tangled (run 1) ***B***-fields. For the helical geometry, the three SEDs are generated by varying θ'_z from 30° to 60° (see Table 2). Top right and bottom: comparison of pulse profiles with those of the base set (run 1) on a linear–linear scale, calculated for the *R* band (top right) and at photon energies of 10 keV (bottom left) and 1 GeV (bottom right).

bands peak sooner and last for a slightly shorter duration than their base set counterparts due to internal light travel time effects and their corresponding boosting in the observer's frame (see Paper I). The exact opposite happens for a larger viewing angle.

For a magnetic field oriented perpendicular to the jet axis, the variation of the angle θ'_{xy} (see Figure 1) does not significantly impact the SEDs and light curves of the blazar in comparison to that of run 1 while keeping the viewing angle the same. This is expected because a variation in the angle that the ***B***-field makes in the x'–y' plane of the cylinder brings about a minor change in the value of the pitch angle, thereby maintaining profiles similar to that of the baseline model. However, the corresponding $\sin\chi'_{\rm feed}$ is 1 for this case. Thus, the SSC emission gets impacted slightly, as can be seen in the top left panel of Figure 10 for the case of perpendicular geometry. The CDF becomes smaller for higher values of θ'_{xy} because for a larger value of θ'_{xy}, the corresponding value of $\sin\chi'$ increases (see Equation (5) for a value of $\theta'_z = 90°$), thereby increasing the synchrotron component and reducing the CDF.

For both parallel and perpendicular cases as well, the presence of a disordered component dilutes the effects of an ordered field in a similar way as discussed above (see bottom left panel of Figure 10).

4.2. Variation of θ'_z

Figure 8 shows the impact of changing θ'_z on the SEDs and SVPs of the blazar for a purely helical field. As described in Section 2.2, this is the angle that the field lines make with the jet or z'-axis. A value of $\theta'_z = 0°$ reproduces the case of a parallel geometry, whereas that of $\theta'_z = 90°$ replicates the toroidal case.

From the figure, it can be seen that as the helicity of the field constrains the corresponding $\sin\chi'$ value (see Table 2), the overall flux level of the SED increases and the CDF decreases while shifting the location of $\nu_{\rm cutoff}$ to higher values with increasing θ'_z. The SH in the X-ray range also gets impacted by the geometry of the field. The X-ray spectrum in the 2–10 keV range becomes softer because it now includes a more dominant contribution from the synchrotron component. On the other hand, as expected, the spectrum in the range of the Fermi-LAT (0.1–200 GeV) retains the same hardness as that of run 1. The slight variation in the flux level of the SSC component is in accordance with the value of $\sin\chi'_{\rm feed}$ as shown in Table 2.

The flare profiles across all energy bands are primarily governed by the ***B***-field topology. As the helicity of the field loosens, the amplitudes of all synchrotron-dominated flares rise and become higher compared to their run 1 counterparts. However, the amplitudes of the SSC-dominated flares are either below or above their run 1 counterparts, depending on the

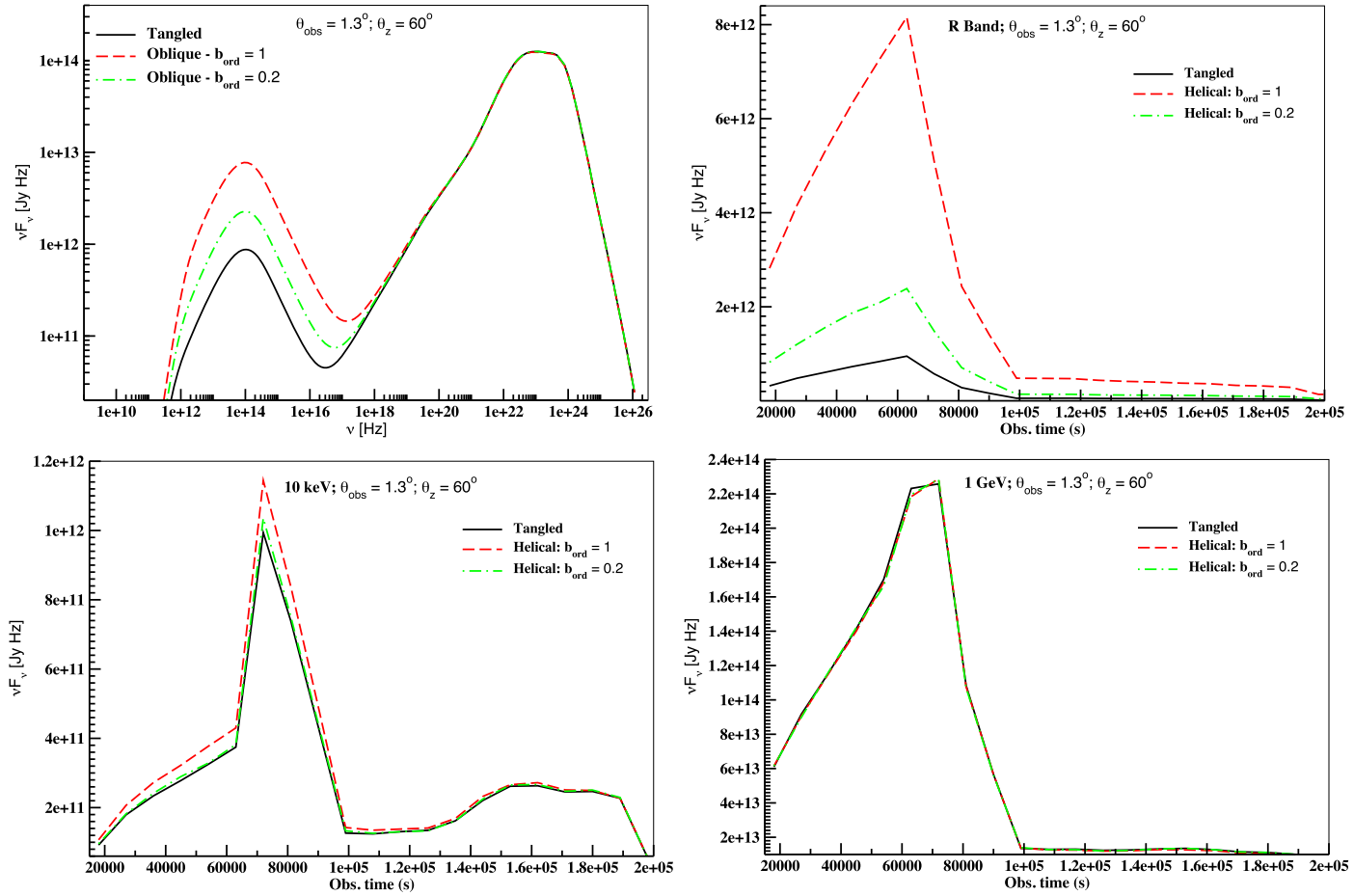

Figure 9. Left: comparison of the time-averaged SEDs of a blazar for a purely helical field (run 3c; $b_{\rm ord} = 1$) with the disordered component included (run 3c; $b_{\rm ord} = 0.2$) and tangled (run 1) ***B***-fields. Right: comparison of light curves obtained from run 3c, with and without the disordered component, for a helical geometry and tangled ***B***-field. Flare profiles are calculated at *R*-band (top right), 10 keV (bottom left), and 1 GeV (bottom right) photon energies. The plot is shown on a linear–linear scale. Compared to run 1, the overall flare profiles are exactly the same for the case of the disordered component, but the flux levels of synchrotron- and SSC-dominated flares (*R* band and 10 keV, respectively) are slightly higher. However, the effect is less compared to their counterparts obtained using a purely helical field.

value of $\sin\chi'_{\rm feed}$, whereas none of the EC-dominated flares are impacted by the field geometry at all (see Figure 8).

Similar to what has been described in Section 4.1, the inclusion of partially ordered ***B***-fields dilutes the impact of a purely helical field on the SED and SVPs of the blazar. However, the reduction of the effect of a purely helical field is not as significant as in the case of an oblique geometry. As an example, Figure 9 shows the comparison of the impact on the SED and SVPs of the generic blazar from run 3c for a purely helical field ($b_{\rm ord} = 1$) and after including the disordered ***B***-field component ($b_{\rm ord} = 0.2$). As can be seen, the overall profiles of the SED and SVPs of the blazar for the case of the disordered component are similar to that of run 1. However, the flux level of the synchrotron-dominated region of the SED and SVPs (*R*-band light curve) is higher compared to its run 1 counterpart but lower than that of a purely helical field. This implies that a helical field can play an important role, even in the presence of a disordered component, in significantly affecting synchrotron emission, in comparison to an oblique field topology.

As discussed in Joshi et al. (2016), for a toroidal ***B***-field, $\sin\chi'$ has an inverse relationship with $\theta_{\rm obs}$ (see Equation (11)). Hence, a smaller $\theta_{\rm obs}$ results in a larger value of $\sin\chi'$. This remains true for as long as the viewing angle is within the superluminal cone of the source corresponding to its BLF, which is the case here. Hence, the flux level of the synchrotron component rises for all viewing angles. For a smaller viewing angle, $\nu_{\rm syn}^{\rm peak}$ shifts to higher frequencies, whereas it shifts to lower values for a larger one. For a viewing angle equal to that of run 1, the location of $\nu_{\rm syn}^{\rm peak}$ remains the same. However, $\nu_{\rm cutoff}$ shifts to higher frequencies compared to its run 1 counterpart for all viewing angles considered here due to a larger synchrotron component. Similar to the case of a parallel ***B***-field, the SSC component is guided by radiation feedback in addition to Doppler boosting. Hence, its corresponding flux level is slightly higher in comparison to its run 1 counterpart despite receiving the same amount of Doppler boosting for the case of the same viewing angle. The CDF of the source gets affected the most, becoming smaller with larger viewing angle. The SH of the X-ray and Fermi ranges, along with the light-curve profiles, gets affected in a similar way as discussed for the case of a purely helical ***B***-field. In addition, the impact of including a disordered component of the ***B***-field on the SED and SVPs of the generic blazar for this geometry is similar to that of a helical one (see left panels of Figure 10).

5. Discussion

Signatures of the orientations of the ***B***-field, which have been studied here, can be extracted by understanding the impact of a

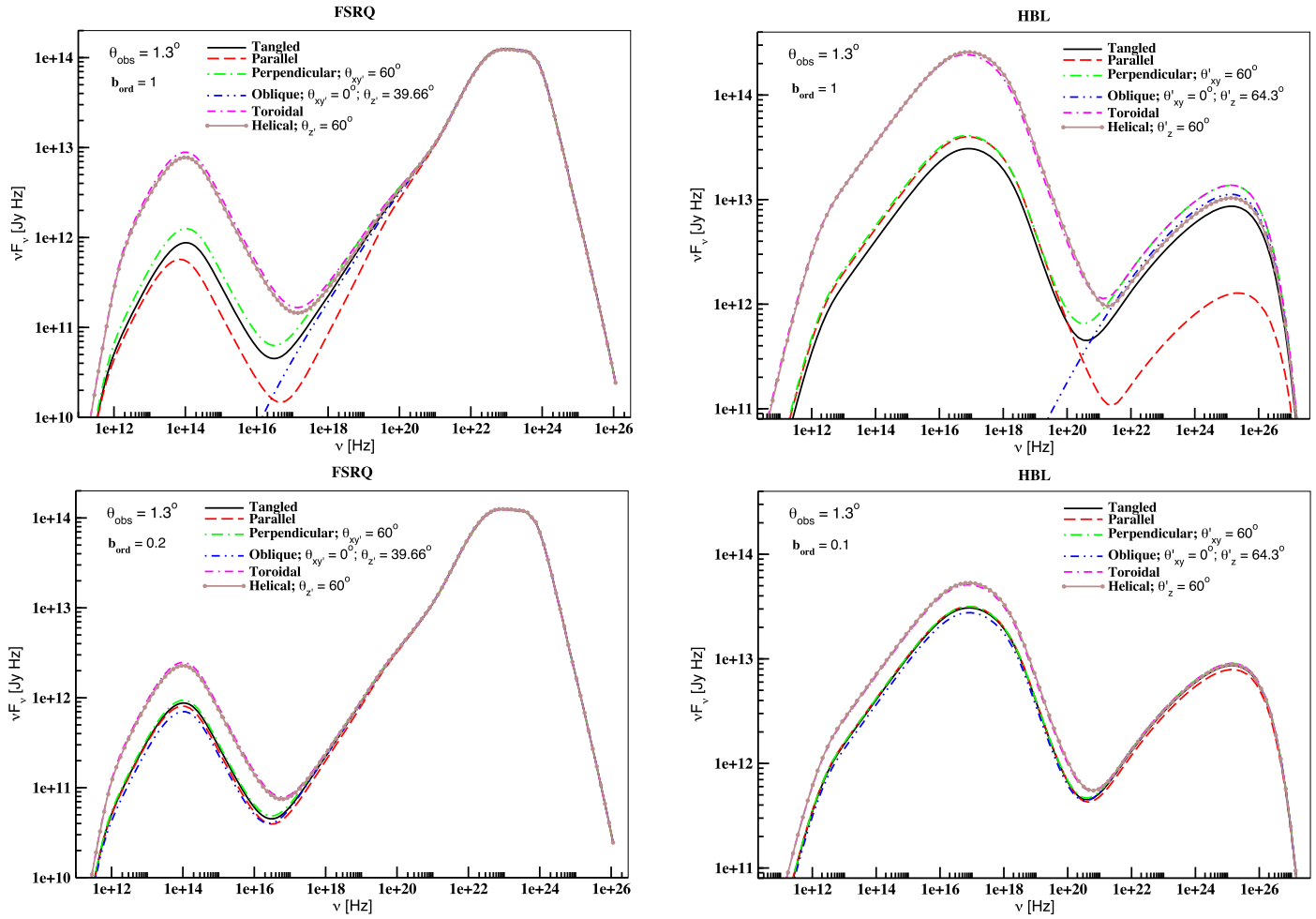

Figure 10. Comparison of time-averaged SEDs of a generic FSRQ-type (left) and an HBL-type (right) blazar for all geometries of ***B***-fields considered here. The generic FSRQ-type blazar corresponds to 3C 454.3, whereas the SEDs for the HBL-type blazar were generated using the redshift of Mrk 421. The time-averaged SEDs shown here are for certain combinations of θ'_{xy} and θ'_{z}, as indicated in the legends. The top panels show results for purely ordered fields ($b_{ord} = 1$), whereas the bottom panels are for partially ordered fields included with values of b_{ord} corresponding to their source type.

particular geometry on the corresponding SED and SVPs of a source coupled with its polarimetric behavior. Here we discuss a few scenarios that can be used to decipher the field geometry in blazars.

The presence of a purely parallel ***B***-field in a source can be gauged from its perpendicular polarization, as indicated by its electric-field vector position angle (EVPA). Such a behavior has been exhibited by blazars such as OJ 248 and PKS 1510–08, where, over a period of about 24 hr, the corresponding $P(\%)$ went down and the EVPA became $\sim 90°$, while their viewing angle and Doppler boosting factor remained the same. This implies a temporary alignment of the ***B***-field close to the jet axis at subparsec or parsec scales, probably due to magnetic reconnection, before it reorients itself to its original position. The lowering of $P(\%)$, however, is an indication of the presence of a disordered ***B***-field component in the system. Including the orientation of the magnetic field also leads to some effects that have to be addressed in order to correctly calculate the SSC radiation from the emission region. These effects arise because the radiation field as seen by each zone is not always the same as that seen by an observer. In the case of a purely parallel ***B***-field, "blind spots" can arise when electrons in a particular zone are not able to see the synchrotron radiation coming from the adjacent zones because the magnetic field is aligned parallel to the direction of incoming photon travel. In that case, electrons do not upscatter incoming synchrotron photons from adjacent zones to produce SSC radiation, and reduced SSC emission is observed from that zone. This effect is even more pronounced for SSC-dominated sources (see the right panels of Figure 10), where its presence greatly reduces the corresponding SSC flux for the reasons stated in Section 4.1. However, as can be seen from the bottom panels of the figure, the overall effect of a purely parallel ***B***-field is significantly diluted in the presence of a disordered field component. Given that typical values of $P(\%)$ for blazars are around a few tens of percent, the corresponding fraction of the ordered component of the field is usually not very high. As a result, the impact of a parallel ***B***-field on the observational signatures of blazars will be hard to decipher in the presence of a disordered component.

The observational signatures of a purely oblique ***B***-field could vary depending on the combination of angles that the field would make with respect to our line of sight and the jet axis. As shown in Section 4.1 and discussed in Section 2.2, certain combinations of various parameters could result in values of $\sin\chi'$ that are nearly zero. Such combinations are essentially governed by the sinusoidal form of the pitch angle equation for the oblique case (see Equation (5)). A nearly zero

value of $\sin\chi'$ implies a very low flux of the synchrotron component in the SEDs of a blazar, especially when the $\boldsymbol{B}$-field is aligned along our line of sight. In this scenario, since the $\boldsymbol{B}$-field is uniform and pointing at the observer, the observer does not see the synchrotron radiation, but the electrons in that region do, thereby producing SSC radiation with observable flux levels (see top panels of Figures 6 and 10). This is because the directionality of the magnetic field creates a dissimilarity in the radiation field seen by an observer versus that by electrons in the emission region, and the observer only sees inverse Compton–scattered radiation coming from the region. Such a scenario can be used to explain the appearance of some γ-ray "orphan flares" observed in a few blazars (Krawczynski et al. 2004). For the blazar PKS 1510–08, a similar state was observed for a period of roughly 5 days starting around 2009 April 23 (Marscher et al. 2010a, 2010b), when a γ-ray flare (#7 in Figure 2 of Marscher et al. 2010a) was observed but a quiescent optical emission was recorded. As discussed in Marscher et al. (2010a), the general trend of the photometric behavior of this blazar for that time period can be explained by invoking a helical $\boldsymbol{B}$-field. But the possibility of an oblique $\boldsymbol{B}$-field being responsible for the photometric behavior of the source, as exhibited in flare #7 of Figure 2 in Marscher et al. (2010a), cannot be ruled out. This is because it is possible for such orientations to arise temporarily upon the passage of shock fronts through the jet while stretching the loop of a preexisting helical field in the process. Hence, such topologies, if present, could be responsible for some short-lived emission, such as a flare of the source, and not its long-term behavior. However, as discussed above, the presence of a partially ordered field greatly reduces the effect of an oblique field on the observational signatures of a blazar (see bottom panels of Figure 10). This implies that the possibility of using a leptonic model to explain a γ-ray "orphan flare" can only work for an oblique field with a high $b_{\rm ord}$ value. For relatively low values of $b_{\rm ord}$, hadronic models have a better chance of reproducing TeV orphan flares through scenarios such as the synchrotron mirror model (Böttcher 2005) or the Wien fireball model (Fraija 2015). Hence, unlike hadronic models that require a high kinetic luminosity and/or $\boldsymbol{B}$-field value, the main requirement of a leptonic model in explaining a γ-ray orphan flare is that the $\boldsymbol{B}$-field should be oblique and highly ordered. Of course, the identification of a suitable set of physical parameters to successfully reproduce a spectral state remains common to both types of jet model.

We also note that one of the behaviors observed during the 2015 June flare of blazar 3C 279 (Fraija et al. 2019) could be explained using the combined effect of ordered and disordered components. A value of $P(\%) > 20\%$ was observed for the source during that time, along with an increase in synchrotron flux. As can be seen from the bottom left panel of Figure 10, an oblique geometry with $b_{\rm ord} \geqslant 0.2$ can be invoked to obtain a CDF $\sim$ 100, a shift in $\nu_{\rm syn}^{\rm peak}$ to $\sim 10^{14}$ Hz, and the corresponding $\nu_{\rm EC}^{\rm peak} \sim 10^{23}$ Hz to reproduce the state observed during that flare (see bottom panels of Figure 10 of Fraija et al. 2019).

Helical fields are widely invoked to explain many features associated with observed polarized emission from blazars. Such fields might persist over larger distances; however, the contribution to the total magnetic field strength might change with distance. In terms of observational signatures, it is difficult to distinguish a toroidal from a helical $\boldsymbol{B}$-field. They both have similar impacts on the SEDs and SVPs of blazars. As discussed in Section 4.2, the CD of the source decreases while the X-ray range spectrum becomes slightly softer in both cases compared to their base set counterparts. The main impact of this geometry is that it enhances the synchrotron emission of the source compared to its tangled $\boldsymbol{B}$-field counterpart. Even though it is difficult to distinguish the two types of $\boldsymbol{B}$-fields based on their observational signatures, it is interesting to note that such fields can play an important role in shaping the emission emanating from the jets of some of the blazars that exhibit a broader synchrotron component and are also softer in the 2–10 keV X-ray range. Contrary to the case of an oblique field, the presence of a disordered $\boldsymbol{B}$-field component for helical and toroidal geometries does not significantly reduce their impacts on the SEDs and SVPs of blazars. As can be seen from Figure 10, even in the presence of a disordered component with the strength of the ordered component of the field being only 10%–20%, the impact on the synchrotron-dominated emission is significant enough compared to its tangled field counterpart that the presence of such fields in the jets can be deciphered using the observational signatures of blazars.

As far as the impact of $\boldsymbol{B}$-field geometry across various subclasses of blazars is concerned, we do not see any difference in the way a particular field topology manifests itself in one subclass versus another. As can be seen from Figure 10, this is expected because the manifestation of the orientation of the field on synchrotron radiation is independent of the nature of the source. However, the level to which the corresponding synchrotron flux level of the source will get affected is indeed dependent on the nature and will vary from one source to another. In Figure 10, we compare the impact of purely and partially ordered parallel, perpendicular, oblique, toroidal, and helical $\boldsymbol{B}$-fields with that of a tangled field for certain chosen combinations of $\theta'_{\rm xy}$ and/or $\theta'_{\rm z}$ for two subclasses of blazars. The generic blazar chosen to represent the subclass of flat-spectrum radio quasars (FSRQs) is the same as that considered for this study, whereas that for the subclass of BL Lac–type objects is a generic blazar with the redshift of Mrk 421, which is a high-frequency peaked BL Lac (HBL) object. The value of $b_{\rm ord}$ considered for the case of HBL is 0.1, which is the typical value of $P(\%)$ for Mrk 421 (Fraija et al. 2017). The overall impact of all geometries on both subclasses is indeed the same for both cases, with variations in synchrotron flux level arising due to differences in the values of Doppler factors and other physical parameters of the two sources. However, since the HE component of most HBLs tends to be SSC-dominated, the impact of a purely parallel $\boldsymbol{B}$-field is much more pronounced compared to its counterpart in FSRQs for the reasons explained above. On the other hand, this effect is significantly reduced in the presence of a partially ordered parallel field, as described in Section 4. The resultant SEDs and light curves look similar to those obtained using a tangled $\boldsymbol{B}$-field for both subclasses.

6. Conclusions

In this paper, we have carried out a parameter study to understand the effects of a purely ordered magnetic field and the combined effects of ordered and disordered components of the $\boldsymbol{B}$-field on blazar jet emission and compare their respective outcomes to that of a tangled $\boldsymbol{B}$-field. The goal of our study is to relate the geometry of the field, in the absence and presence of a disordered component, to the observational properties of blazars, such as SEDs and SVPs, and provide a framework for inferring intrinsic differences in the relevant physical

parameters. We quantify the impact of the field geometry in terms of the change in the SH, CD, and location of the peak synchrotron flux and cutoff frequencies.

We have carried out this study in two parts. In Part 1, we assume a purely ordered $\boldsymbol{B}$-field to thread the multizoned emission region. This assumption lets us to calculate either the maximum or the minimum impact that a certain geometry can have on the SEDs and SVPs of a blazar. For example, a longitudinal field pointing right along the line of sight gives zero synchrotron but normal SSC emission, while an ordered field that is at some modest angle to the line of sight has similar synchrotron and SSC ratios as that of the tangled field case. Hence, depending on the angle that the field makes with respect to our line of sight, we obtain either a lower or an upper limit to the impact of the $\boldsymbol{B}$-field topology on the observational signatures of blazars. We assume the emission to be negligible before the passage of shocks, and with the passage of shocks, the $\boldsymbol{B}$-field becomes compressed and ordered in every zone of the emission region (see Section 3).

The SSC emissivity of the generic source is calculated using the modified synchrotron emissivity, which includes the dependence on the pitch angle. As pointed out in Section 2.2, in order to calculate the SSC emission in the presence of a $\boldsymbol{B}$-field, we need to take into account the way the electrons in a particular zone perceive the optically thin and anisotropic synchrotron radiation that the zone receives from the adjacent zones on either side in the form of radiation feedback. This results in a combination of angle-averaged and anisotropic synchrotron radiation being used for the calculation of the subsequent SSC emission from a particular radiating zone. Hence, the SSC emission is not adversely affected by the presence of an ordered $\boldsymbol{B}$-field in the emission region as long as the corresponding radiation feedback is not zero. This is because the $\boldsymbol{B}$-field orientation changes only the directionality of the synchrotron radiation field and does not impact its overall radiation energy density. For such cases, the SSC flux remains approximately the same as it would have in the presence of a tangled magnetic field. However, the situation changes when the radiation feedback, as seen by a particular radiating zone, becomes zero. As can be seen from the top panels of Figure 10, for the case of a purely parallel field, the corresponding SSC flux goes down, and the impact is significant for SSC-dominated sources.

Our findings in Section 4 confirm some of the general trends in the SEDs of a blazar that are expected from the presence of a purely ordered $\boldsymbol{B}$-field, such as enhancement of the synchrotron component in the presence of highly ordered (e.g., toroidal, helical) $\boldsymbol{B}$-fields. The presence of such fields directly affects the CDF of the source and makes the X-ray spectrum softer. In addition, some of the results demonstrate the peculiarities that the geometry of the field can have on the SEDs and SVPs of a blazar. This can be seen especially for the case of a purely oblique geometry, as discussed in Section 4.1. As shown in Figure 6, a combination of θ'_z and θ'_{xy} for the choice of our input parameters can lead to a scenario where the synchrotron emission is suppressed (or absent) while the inverse Compton component stays the same in comparison to that of the base set. This increases the overall CDF of the source and the SH of the X-ray spectrum. Such a scenario could explain some HE orphan flares observed in some blazars. Similarly, in the case of a parallel $\boldsymbol{B}$-field (Section 4.1), the synchrotron component follows an inverse relationship with Doppler boosting due to the relationship of the corresponding pitch angle with the viewing angle. In addition, the electrons in a particular radiating zone do not see the synchrotron radiation coming from adjacent zones. This creates blind spots for the electrons in that zone and results in reduced SSC emission (see the top panels of Figure 10). It also directly impacts the CDF of the source and makes the X-ray spectrum harder compared to the tangled field case.

The impact of $\boldsymbol{B}$-field orientation on various subclasses of blazars, such as FSRQs and HBLs, was also studied. As expected, the geometry has similar effects on SEDs and SVPs across the two subclasses. However, the degree of impact varies according to the difference in their Doppler boosting, the values of the relevant physical parameters, and the nature of the source itself—whether it is an SSC-dominated source (such as an HBL) or an EC-dominated one.

In Part 2, we included a disordered component of the $\boldsymbol{B}$-field in the calculation of synchrotron emission and investigated the combined effects of purely and partially ordered components of the field for a given geometry on the SEDs and SVPs of blazars. As discussed in Section 5 and seen in the bottom panels of Figure 10, the impact of an ordered $\boldsymbol{B}$-field on the SED and SVPs is reduced upon the inclusion of a disordered component, and the plots look similar to those obtained using a tangled $\boldsymbol{B}$-field. This holds true for parallel, perpendicular, and oblique geometries. For helical and toroidal fields, the effect is reduced but to a lesser degree, and the amplitude of synchrotron-dominated emission for blazars under this scenario continues to be higher compared to that obtained using a tangled field. In addition, this trend is maintained across both subclasses of blazars investigated here.

We point out that our model does not account for any anisotropy in the electron population that might be induced due to the presence of an ordered magnetic field. However, there will be no systematic anisotropy in the electron momentum losses, so the assumption of an isotropic electron distribution is justified.

Exploring the structure of the magnetic field and particle acceleration in the jets of blazars is one of the essential steps toward understanding phenomena near black holes. In this work, we have addressed this aspect by including the magnetic field direction in our existing multizone time-dependent leptonic jet model MUZORF. This study is a first step toward exploring the combined effects of ordered and disordered magnetic fields on the observational properties of blazars. The effects of the evolution of $b_{\rm ord}$ as the emitting volume propagates through the jet will be addressed in future work.

We thank the anonymous referee for insightful and constructive comments. We thank Drs. Svetlana Jorstad, Ranjiv Misra, John Wardle, Lorenzo Sironi, and Atish Kamble for useful discussions and comments. We thank Dr. Jack Steiner for help with gaining access to computational facilities. We thank the Boston University Shared Computing Cluster (SCC) located at the Massachusetts Green High Performance Computing Center (MGHPCC) for providing high-end computational facilities where all of the simulations were performed. We thank the NASA High-End Computing (HEC) Program for providing us with computational facilities where part of the simulations reported here were performed. The Boston University effort on this project was

supported by NASA through Fermi grants 80NSSC17K0650, NNX11AQ03G, and NNX12AO59G and National Science Foundation grant AST-1615796. M.B. acknowledges support by the South African Research Chairs Initiative (grant No. 64789) of the Department of Science and Technology and the National Research Foundation of South Africa.

ORCID iDs

Manasvita Joshi https://orcid.org/0000-0003-1134-7352
Alan P. Marscher https://orcid.org/0000-0001-7396-3332
Markus Böttcher https://orcid.org/0000-0002-8434-5692

References

Ackermann, M., Ajello, M., Atwood, W. B., et al. 2015, ApJ, 810, 14
Aleksić, A., Ansoldi, S., Antonelli, L. A., et al. 2014, A&A, 567, 135
Aller, H. D., Aller, M. F., & Hughes, P. A. 1985, ApJ, 298, 296
Beckwith, K., Hawley, J. F., & Krolik, J. H. 2008, ApJ, 707, 428
Böttcher, M. 2005, ApJ, 621, 176
Böttcher, M., & Reimer, A. 2004, ApJ, 609, 576
Cawthorne, T. V., & Cobb, W. K. 1990, ApJ, 350, 536
Cawthorne, T. V., & Wardle, J. F. C. 1988, ApJ, 332, 696
Ciprini, S. 2016, ATel, 9869
Crusius, A., & Schlickeiser, R. 1986, A&A, 164, L16
D'Arcangelo, F. D., Marscher, A. P., Jorstad, S. G., et al. 2009, ApJ, 697, 985
De Villiers, J.-P., Hawley, J. F., Krolik, J. H., & Hirose, S. 2005, ApJ, 620, 878
Fraija, N. 2015, APh, 71, 1
Fraija, N., Benitez, E., Hiriart, D., et al. 2017, ApJS, 232, 7
Fraija, N., Benitez, E., Hiriart, D., et al. 2019, ApJS, 245, 18
Gabuzda, D. C. 2017, Galax, 5, 11
Gabuzda, D. C., Murray, E., & Cronin, P. 2004, MNRAS, 351, L89
Gabuzda, D. C., Rastorgueva, E. A., Smith, P. S., & O'Sullivan, S. P. 2006, MNRAS, 369, 1596
Gabuzda, D. C., Sitko, M. L., & Smith, P. S. 1996, AJ, 112, 1877
Graff, P. B., Georganopoulos, M., Perlman, E. S., & Kazanas, D. 2008, ApJ, 689, 68
Gupta, A. C., Mangalam, A., Wiita, P. J., et al. 2017, MNRAS, 472, 788
Homan, D. C., Lister, M. L., Aller, H. D., Aller, M. F., & Wardle, J. F. C. 2009, ApJ, 696, 328
Hughes, P. A., Aller, H. D., & Aller, M. F. 1989, ApJ, 341, 54
Jamil, O., & Böttcher, M. 2012, ApJ, 759, 45
Jorstad, S. G., Marscher, A. P., Lister, M. L., et al. 2005, AJ, 130, 1418
Jorstad, S. G., Marscher, A. P., Stevens, J. A., et al. 2007, AJ, 134, 799
Jorstad, S. G., Marscher, A. P., Smith, P. S., et al. 2013, ApJ, 773, 147
Joshi, M., & Böttcher, M. 2007, ApJ, 662, 884
Joshi, M., & Böttcher, M. 2011, ApJ, 727, 21
Joshi, M., Marscher, A. P., & Böttcher, M. 2014, ApJ, 785, 132
Joshi, M., Marscher, A. P., & Böttcher, M. 2016, Galax, 4, 45
Kardashev, N. S. 1962, SvA, 6, 317
Krawczynski, H., Hughes, S. B., Horan, D., et al. 2004, ApJ, 601, 151
Laing, R. 1980, MNRAS, 193, 439
Lister, M. L., & Smith, P. S. 2000, ApJ, 541, 66
Lyutikov, M., Pariev, V. I., & Gabuzda, D. C. 2005, MNRAS, 360, 869
Mahmud, M., & Gabuzda, D. C. 2007, in Proc. Modern Radio Universe Conf., From Planets to Dark Energy (Trieste: SISSA), 74
Marscher, A. P. 2014, ApJ, 780, 87
Marscher, A. P., Jorstad, S. G., D'Arcangelo, F. D., et al. 2008, Natur, 452, 966
Marscher, A. P., Jorstad, S. G., Larionov, V. M., et al. 2010a, ApJL, 710, 126
Marscher, A. P., Jorstad, S. G., D'Arcangelo, F. D., et al. 2010b, arXiv:1002.0806
McKinney, J. C., & Gammie, C. F. 2004, ApJ, 611, 977
McKinney, J. C., Tchekhovskoy, A., & Blandford, R. 2012, MNRAS, 423, 3083
Moderski, R., Sikora, M., & Błażejowski, M. 2003, A&A, 406, 855
Mukherjee, R. 2017, ATel, 10051
Rybicki, G. B., & Lightman, A. P. 1979, Radiative Processes in Astrophysics (New York: Wiley)
Sokolov, A., Marscher, A. P., & McHardy, I. M. 2004, ApJ, 613, 725
Wentzel, D. G. 1969, ApJ, 157, 545
Zhang, H., & Böttcher, M. 2013, ApJ, 774, 18
Zhang, H., Chen, X., & Böttcher, M. 2014, ApJ, 789, 66